Serpentinization and Associated Hydrogen and Methane Fluxes at Slow Spreading Ridges

Mathilde Cannat, Fabrice Fontaine, and Javier Escartin

Equipe de Géosciences Marines, CNRS-UMR7154, Institut de Physique du Globe, Paris, France

We estimate that domains with frequent outcrops of mantle-derived ultramafics represent about 20–25% of the seafloor created at ridges spreading at rates less than 40 mm a^{-1} and form at asymmetric detachment faults along about 14,660 km of the present-day ridge system. Ridge serpentinization extends to a maximum of 3 to 4 km into the footwall of axial detachment faults and consumes about 0.18 km^3 of fresh peridotite per year. We estimate serpentinization-related hydrogen and methane fluxes with two independent methods, one based on the proportion of serpentine in slow spreading crust, and the other based on estimated regional hydrothermal heat fluxes. Our results yield "initial" (prior to methane production) hydrogen fluxes ranging between 0.33 and 4.1 10^7 mol a^{-1} and per kilometer of ridge axis, in domains where mantle exhumation occurs and for the average exhumation rate of 11.4 mm a^{-1}. Geological considerations lead us to prefer an intermediate value around 10^7 mol a^{-1} km^{-1}, corresponding to a global hydrogen flux of about 16.7 10^{10} mol a^{-1}. Based on methane/hydrogen concentration ratios in ultramafic-hosted vent fluids, this would correspond to a global methane flux of about 0.4 megaton (Mt) a^{-1}. These estimates correspond to averages over the time it takes for the exhumed material to leave the axial domain. In the discussion, we relate fluid circulation, serpentinization, and hydrogen production, to the distribution of brittle fracture and faulting in the detachment fault's footwall. We distinguish two principal settings, depending on whether melt is being emplaced and cooled in this fractured and permeable footwall domain.

Q1

Q2

1. INTRODUCTION

Mantle-derived ultramafic rocks form massive outcrops in the walls of the axial valley of slow spreading ridges (spreading rates <40 mm a^{-1}), most commonly near axial discontinuities [*Aumento and Loubat*, 1971; *Cannat*, 1993; *Dick*, 1989; *Karson et al.*, 1987]. Off-axis, they crop out in the thinner crust domains near the traces of these axial discontinuities [*Cannat et al.*, 1995; *Tucholke and Lin*, 1994]. Serpentinized peridotites also occur at ultraslow spreading ridges [*Dick*, 1989; *Dick et al.*, 2003; *Michael et al.*, 2003; *Seyler et al.*, 2003], where they locally form very extensive outcrops, over distances of tens of kilometers. Models for the exhumation of these mantle-derived rocks involve large offset normal faults [*Karson*, 1991; *Tucholke and Lin*, 1994] and a cold axial thermal regime that prevents the formation of steady-state melt reservoirs at crustal levels [*Cannat*, 1993; *Sleep and Barth*, 1997]. In the extreme case of melt-poor and ultraslow ridges, volcanism may be suppressed

TITLE
Geophysical Monograph Series XXX
XXXXXXXXXXXXXXXXXXXXXXXXXXX
10.1029/2008GM000760

altogether [*Cannat et al.*, 2006]. Even in these extreme cases, however, the oceanic seismic crustal thickness is nonzero [*Jokat et al.*, 2003; *Minshull et al.*, 2006; *Muller et al.*, 1999], and serpentinization is discussed as a mechanism to reduce mantle seismic velocity and density to crustal values [*Cannat*, 1993; *Carlson*, 2001; *Carlson and Miller*, 1997; *Christensen*, 1972; *Hess*, 1962; *Minshull et al.*, 1998].

The concept of a partly serpentinized oceanic crust dates back to the early years of plate tectonics [*Hess*, 1962], before most axial ultramafic outcrops had been discovered. It was largely abandoned over the next 20 years, while the dominantly basaltic nature of the oceanic crust was evidenced [*Casey*, 1981; *Ophiolites*, 1972]. It came back in the 1990s, however, following detailed studies of the geological variability of the Mid-Atlantic Ridge (MAR) crust [*Aumento and Loubat*, 1971; *Cannat*, 1993; *Karson and Dick*, 1984; *Karson et al.*, 1987]. There is now a consensus that slow spreading oceanic crust locally contains a serpentinized mantle-derived component, but the questions of how locally, and how much, are still debated [*Carlson and Miller*, 1997; *Minshull et al.*, 1998]. The interest in these questions has been renewed in recent years because minerals produced by the hydrated alteration of peridotite have a strong effect on rheology [*Escartin et al.*, 2008; *Escartín et al.*, 1997, 2001; *Moore and Lockner*, 2008; *Raleigh and Paterson*, 1965; *Reinen et al.*, 1991] and because of the growing evidence that serpentinization processes contribute significantly to the overall hydrothermal fluxes at and near slow spreading ridges [*Rona et al.*, 1992; *Bougault et al.*, 1993; *Charlou and Donval*, 1993; *Fruh-Green et al.*, 2003; *Kelley et al.*, 2001]. Serpentinization of abyssal peridotites has been shown to produce large volumes of hydrogen [*Charlou et al.*, 2002], part of which combines with carbon [*Berndt et al.*, 1996], and produces methane anomalies in the water column [*Charlou and Donval*, 1993; *Charlou et al.*, 1998]. These hydrogen and methane fluxes provide energy to microbial systems within the substratum and at the vents [*Shock and Holland*, 2004]. The amount of hydrogen and methane produced by serpentinization should therefore influence how much biomass can be produced autotrophically at mid-ocean ridges. The remaining hydrogen is more rapidly reacted in seawater and does not therefore reside in the water column [*Kadko et al.*, 1990]. Methane resides longer in diluted hydrothermal plumes above the vents [*Kadko et al.*, 1990], so that the most dramatic evidence for venting of large volumes of serpentinization-related fluids at slow spreading mid-ocean ridges comes from the widespread methane anomalies in the water column [*Charlou and Donval*, 1993; *Charlou et al.*, 1998].

Serpentine-hosted hydrothermal vents constitute specific ecosystems and provide unique conditions, which may resemble the conditions that prevailed in the Early Earth and allowed the emergence of life [e.g., *Shock and Holland*, 2004]. How much serpentinization occurs in the oceanic crust is also an issue of interest for subduction studies, both for rheological reasons [*Brudzinski et al.*, 2007] and because prograde metamorphism of subducted serpentines may be a critical process for fluid and chemical transfers from the subducted slab to the mantle wedge [*Ulmer and Trommsdorff*, 1995]. Finally, active mantle exhumation and serpentinization at slow ridges may provide clues to understand similar processes, which occurred at the Continent Ocean Transition of some continental margins [*Beslier et al.*, 1990; *Boillot et al.*, 1989; *Whitmarsh et al.*, 2001].

In this chapter, we propose an overview of the geological and geophysical observations, mostly from the MAR and Southwest Indian Ridge (SWIR), which can be used to constrain estimates of (1) how much mantle-derived material there is in slow and ultraslow spreading oceanic crust, as it leaves the ridge axis and (2) the degree of serpentinization at any given depth in ridge regions that appear to have a large mantle-derived crustal component. Next, we propose two independent methods to estimate the hydrogen and methane fluxes at slow and ultraslow spreading ridges. One method is based on the proportion of serpentine in slow spreading crust, as estimated based on geological and geophysical constraints. A similar approach has been applied by *Skelton et al.* [2005] to serpentinization in the context of continental margins, and by *Sorokhtin et al.* [2001] and *Emmanuel and Ague* [2007], to serpentinization at mid-ocean ridges. As will be shown, our estimates of methane fluxes agree with those of the study of *Emmanuel and Ague* [2007], but we provide a much more thorough exploration of the various assumptions and controlling parameters. Most notably, we show the important effect of the nonlinear relation between the degree of serpentinization, and the production of magnetite and hydrogen [*Oufi et al.*, 2002; *Toft et al.*, 1990]. The other method we use to estimate hydrogen and methane fluxes is based on an estimate of regional hydrothermal heat fluxes and uses hydrogen, methane, and dissolved iron concentrations in fluids from ultramafic-hosted vents. This approach was used by *Kasting and Catling* [2003], based on concentrations in the Lost City ~~(LC)~~ low-temperature vent fluids [*Kelley et al.*, 2001]. We extend it to high-temperature ultramafic-hosted vents, using concentrations measured in fluids of the Rainbow ~~(R)~~ and Logachev ~~(L)~~ hydrothermal fields [*Charlou et al.*, 2002]. We then discuss the assumptions made for each method and compare their results. This leads us to discuss the spatial and temporal variability of serpentinization-related hydrothermal systems at slow spreading ridges, and their links with faulting and magmatic axial processes.

2. HOW MUCH MANTLE-DERIVED MATERIAL IS THERE IN SLOW AND ULTRASLOW SPREADING OCEANIC CRUST?

Estimating how much of the oceanic crust is made of exhumed mantle-derived rocks involves going from scarce and localized dredging or submersible observations, to the regional and global scales. This requires the use of geophysical proxies to map domains that are most likely to include ultramafic seafloor. Conceptual models of mantle exhumation at mid-ocean ridges are also needed as a frame in which to interpret, and tentatively generalize, sampling results. In this section, we give an overview of the use of geophysical proxies and sampling results in three areas of the slow spreading MAR (around 23° and 15°N) and of the ultraslow SWIR (61° to 69°E). These three areas are chosen because they have the best available geological and geophysical constraints. We discuss these constraints in the frame of current conceptual models for mantle exhumation at mid-ocean ridges, and we propose tentative estimates of the proportion of mantle-derived rocks in the crust of these three key areas.

2.1. Extension of Domains With Frequent Ultramafic Outcrops in Slow and Ultraslow Spreading Oceanic Crust

Mantle-derived ultramafic rocks are commonly exposed in regions of slow and ultra slow spreading ridges that have thinner than normal oceanic crust and are therefore inferred to be less magmatically robust [*Cannat*, 1993, 1996; *Dick*, 1989]. In the most common case, these melt-depleted regions correspond to the end of individual ridge segments, within 10 to 20 km of axial discontinuities (Figure 1). In this segment-end context, ultramafic outcrops are mostly restricted to the inside-corner ridge flank (see Figure 1), while the outside-corner ridge flank exposes basalts and doleritic intrusions [*Severinghaus and MacDonald*, 1988; *Tucholke and Lin*, 1994]. With a typical length of 60 km for a MAR segment [*Thibaud et al.*, 1998], and for symmetrical spreading, this preferred setting therefore corresponds to an estimated proportion (A) of about 15% to 30% (half of the total surface accreted along 30% to 60% of the segment length) for the domains with common ultramafic exposures. This estimate can be checked using a combination of gravity data, seafloor morphology, and sampling. Regions with frequent ultramafic outcrops are characterized by less negative gravity anomalies and have a chaotic topography, contrasting with the regular abyssal hills pattern of thicker oceanic crust [*Cannat et al.*, 1995, 1997b]. In the example shown in Figure 2, for the 150 km by 150 km area mapped near the MAR between 21°50′ and 23°40′N, the proportion (A) of the oceanic domains predicted, on the basis of their gravity and topographic signature, to include ultramafic seafloor is about 23% [*Cannat et al.*, 1995].

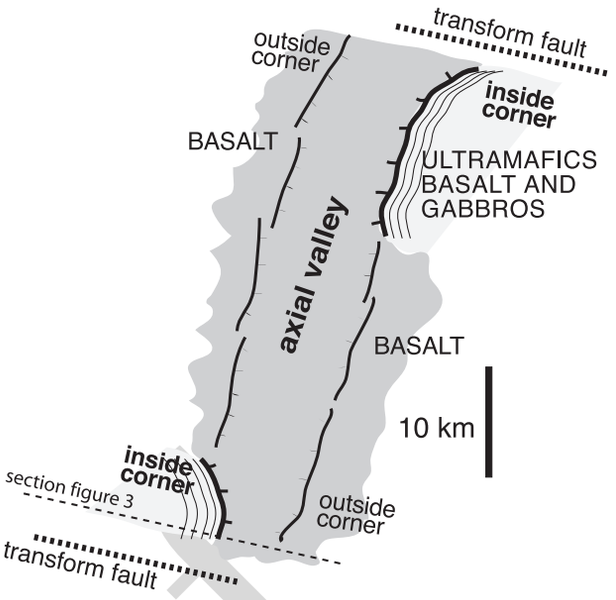

Figure 1. Sketch of a segment of the Mid-Atlantic Ridge (MAR). Basalts crop out in the axial valley floor and in both ridge flanks except in the inside corners, which expose exhumed ultramafics, and variable proportions of gabbros and basalts.

The melt supply averaged over the whole length of MAR ridge segments, as inferred from crustal thickness, is in most cases equivalent to the global average (6- to 7-km-thick fully magmatic crust) [*Chen*, 1992]. This means that mantle exhumation at most ridge segment ends is not associated with a regional melt deficit, but with a local melt deficit due to melt focusing toward ridge segment centers [*Kuo and Forsyth*, 1988; *Lin et al.*, 1990; *Magde et al.*, 1997]. By contrast, and for reasons that are not yet fully understood, the other two areas selected for this overview (MAR around 15°N and SWIR 61° to 69°E) suffer from a regional deficit in melt supply [*Cannat et al.*, 1999b, 2008; *Escartín and Cannat*, 1999; *Fujiwara et al.*, 2003]. These melt-poor regions also expose wider expanses of ultramafic seafloor.

In the 15°N region of the MAR (spreading rate 25 mm a^{-1}) [*Fujiwara et al.*, 2003], chaotic [*Cannat et al.*, 1997b] and locally corrugated seafloor, with frequent ultramafic outcrops, forms in three, up to 80-km-long regions of the ridge axis [*Smith et al.*, 2008]. Ultramafic outcrops in these three ridge regions are not restricted to the ends of ridge segments [*Cannat et al.*, 1997b; *Escartín and Cannat*, 1999] and are commonly found in both ridge flanks, indicating conditions that favor changes in the polarity of axial detachment faults [*Cannat et al.*, 1997b]. Seafloor with a chaotic

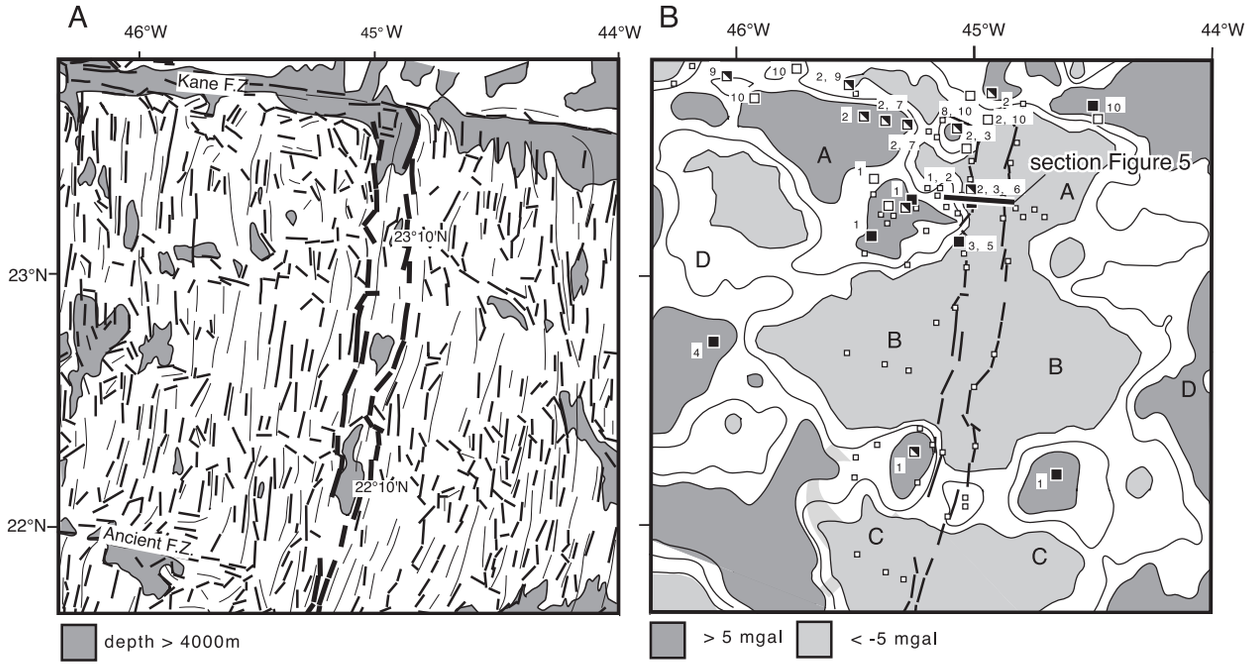

Figure 2. In the 23°N region of the MAR, on-axis and off-axis rock sampling has shown that exhumed ultramafic rocks crop out in seafloor domains, which are characterized by (a) chaotic topography and (b) more positive gravity anomalies, as opposed to the more regular pattern of ridge-parallel abyssal hills, and the less positive gravity anomalies, which characterize domains where only basaltic rocks crop out [after Figures 2 and 3 of *Cannat et al.*, 1995]. Thin and thick lines in Figure 2a correspond to abyssal hills and to larger fault scarps, respectively. Gravity anomalies in Figure 2b are simplified from the residual mantle Bouguer anomaly map of *Deplus et al.* [1992]. Sampling of ultramafic rocks, black squares; of ultramafics and gabbros, black and white squares; of basalts, small open squares. References for sample locations are given by *Cannat et al.* [1995].

or a corrugated topography, positive gravity anomalies, and frequent ultramafic outcrops represents about 40% (*A*) of the near-ridge area mapped between 15°20′ and 16°20′N [*Cannat et al.*, 1997b] and a probably larger proportion of the near-ridge area mapped between 12°50′ and 15°10′N [*Smith et al.*, 2008].

The 61°–69°E region of the ultraslow SWIR (spreading rate: 14 mm a^{-1}) has a very deep seafloor (average axial depth >4700 m) and an average crustal thickness of only 3 to 4 km [*Minshull et al.*, 2006; *Muller et al.*, 1999]. It is inferred to represent a melt-poor end-member for the ridge system worldwide [*Cannat et al.*, 2008] and is comparable to the central part of the Gakkel Ridge in the Arctic [*Michael et al.*, 2003]. It also shares many characteristics with a very oblique portion of the SWIR between 9° and 14°E [*Dick et al.*, 2003]. Domains with common ultramafic outcrops in these regions form corridors that extend on both ridge flanks up to 80 km along-axis [*Cannat et al.*, 2006], similar to what is observed in the 15°N region of the MAR. These domains represent 41% (*A*) of a 400 km by 400 km area mapped between 61° and 66°E [*Cannat et al.*, 2006]. Domains with common ultramafic outcrops in the 61°–69°E region of the SWIR are, however, different from those in the 15°N region of the MAR: corrugated seafloor morphologies are less common (representing only 4% of the total mapped area), and seafloor with a smooth morphology, showing no visible corrugations, and no evidence for a volcanic upper layer, at least at the resolution of shipboard bathymetry, is dominant [*Cannat et al.*, 2006]. This "smooth seafloor" is not found in the 15°N MAR area nor at any other mapped portion of the MAR. It forms at minimal ridge's melt supply, with no or very little axial volcanism [*Cannat et al.*, 2006].

2.2. Proportions of Magmatic Rocks in the Crust of Domains With Frequent Ultramafic Outcrops

Seafloor morphology, and the gravity signature, can be used as proxies to map domains with common ultramafic

outcrops, but do not resolve the proportion of magmatic rocks, which may be mixed with the mantle-derived rocks in the crust of these domains. This magmatic component (*m*) can be estimated from the proportion of magmatic versus mantle-derived lithologies in dredges and along submersible dive tracks. This approach leads to a proposed value of *m* around 35% for both the 23° and 15°N regions of the MAR and of only 10% for the 61°–69°E region of the SWIR [*Cannat et al.*, 2004]. Very extensive sampling in a subset of the 23°N MAR region (between 23°15′ and 23°40′N; Figure 2) suggests that ~~in~~ the magmatic component (*m*), there is about 60% [*Dick et al.*, 2008]. These estimates have large uncertainties attached to them, primarily because available sampling at most locations is insufficient to properly constrain the spatial variability of the magmatic component. Another potential source of errors is that the sampling approach assumes that proportions of magmatic versus mantle-derived lithologies at the seafloor are representative of the deeper crustal levels. In the next paragraphs, we discuss this assumption, and the possible variability of *m* values, in the frame of conceptual models of mantle exhumation and magmatism at slow and ultraslow ridges.

There are two end-member models for mantle exhumation at MAR-type, slow spreading ridges. In one model [*Cann et al.*, 1997; *Karson*, 1990; *Tucholke and Lin*, 1994], mantle exhumation results from large offset normal faulting of a previously formed, fully magmatic crust (Figure 3a). In this interpretation, mantle exhumation (Figure 3b) therefore alternates with periods during which this continuous magmatic crust is formed (Figure 3a), and the proportion of magmatic rocks at the outcrop is not necessarily representative of the deeper crustal levels. In the other model [*Buck et al.*, 2005; *Cannat*, 1993, 1996; *Cannat and Casey*, 1995; *Cannat et al.*, 1997a, 2006; *Dick et al.*, 2008; *Escartin et al.*, 2003; *McCaig et al.*, 2007; *Tucholke et al.*, 2001, 2008], mantle exhumation also results from large offset normal faulting, but faulting affects a composite crust, which forms as exhumation proceeds, through the emplacement of magmatic intrusions (Figure 3c). The hanging wall section includes lavas and shallow magmatic intrusives, and the footwall section comprises exhumed mantle with gabbroic plutons (Figure 3c). In this second model, alternating fully magmatic and amagmatic spreading episodes are not required to explain the large proportion of magmatic rocks sampled next to exhumed ultramafic rocks in our two MAR key areas, and seafloor sampling may be interpreted as representative of the composition of at least the upper 2–3 km of the crust (above the minimum emplacement depth of gabbroic intrusions; Figure 3c). Two mechanisms may, however, cause a spatial variability of the magmatic component (*m*) in this configuration. One is variability of the rate of melt emplacement within the mantle-derived peridotites, as exhumation proceeds, and the other, discussed below, is the initiation of a new detachment fault.

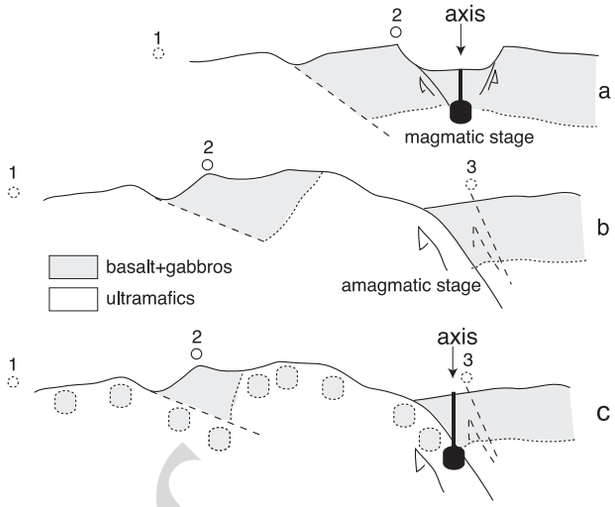

Figure 3. Sketches summarizing the principal aspects of two alternative models for the exhumation of mantle-derived ultramafics at slow spreading ridges (see text). (a and b) The first model involves alternating periods of fully magmatic and fully amagmatic plate separation. We favor (c) the second model which involves melt emplacement in the form of gabbroic intrusions and doleritic dikes, while the ultramafics are being exhumed. These across-axis sections could correspond to the inside-corner setting sketched in Figure 1. Dots labeled 1, 2, and 3 correspond to successive axial normal faults (see text). These sketches show three different ways by which magmatic rocks can be incorporated into domains of frequent ultramafic outcrops: as intrusions (Figure 3c), as faulted sections of magmatic crust formed during magmatic spreading periods (Figures 3a and 3b), and as former portions of the opposite plate, captured by the initiation of a new axial normal fault (Figures 3a–3c). Q3

Individual detachment faults are expected to stop their activity after a few kilometers to a few tens of kilometers of displacement, as bending stresses due to unroofing of the footwall become too high [*Buck*, 1988; *Lavier et al.*, 1999]. A new detachment is then predicted to initiate, in most cases inward from the previous one. It thus captures a section of the hanging wall, exposing volcanic extrusives, doleritic intrusives, and gabbros, before mantle exhumation resumes (Figures 3b and 3c). In the case of the second model of coupled exhumation and magmatism (Figure 3c), this would cause a local increase of the magmatic component (*m*) estimated from seafloor sampling, which may or may not be representative of deeper crustal levels. The resulting local crustal architecture would look locally like the one produced in the first conceptual model (Figure 3b), but would not

correspond to the same alternation of fully magmatic and amagmatic spreading. *Buck et al.* [2005] have proposed that the longest-lasting axial detachment faults develop when the rate of exhumation is equal to the half-spreading rate, the other half being accommodated by magmatism in the hanging wall.

Successive axial detachments may also flip polarity, leading to the exposure of mantle-derived rocks in both ridge flanks [*Cannat et al.*, 1997b, 2006]. This is observed in our two melt-poor key areas (MAR 15°N and SWIR 61°–69°E), where mantle exhumation is not restricted to inside corner-type settings. It is also observed in regions that have a normal melt supply, next to axial discontinuities that have a very small offset (<20 km). This is, for example, the case near the 23°10′ and 22°10′N discontinuities in the 23°N region of the MAR, where the positive gravity anomalies and chaotic topography characteristic of terranes with frequent ultramafic outcrops have formed successively in the two ridge flanks (Figure 2). A possible interpretation is that these discontinuities have themselves repeatedly switched polarity, causing inside corners to become outside corners and back.

2.3. Proportion of Mantle-Derived Ultramafics in Slow and Ultraslow Spreading Oceanic Crust

The 9% estimate (E) published by *Cannat et al.* [2004] for the regional proportion of mantle-derived ultramafics in the crust of the 23°N MAR region (between 21°50′ and 23°40′N; Figure 2) was calculated (equation (1)) for an areal proportion of domains with frequent ultramafic outcrops (A) of 23% (see section 2.1), a magmatic component (m) of 35% in these domains (see section 2.2), a mean regional seismic crustal thickness (C) of 6.8 km [*Purdy and Detrick*, 1986], and a mean gravity-derived crustal thickness in domains with frequent ultramafic outcrops (c) of 4 km [*Maia and Gente*, 1998].

$$E = (1 - m)cA / C. \quad (1)$$

Equation (1) yields E = 20% for the region of the MAR between 15°20′ and 16°20′N [*Cannat et al.*, 2004], for an areal proportion of domains with frequent ultramafic outcrops (A) of 40%, a magmatic component (m) of 35% in these domains, a mean regional seismic crustal thickness (C) of 5.4 km (Detrick and Collins, personal communication, 1998), and a mean gravity-derived crustal thickness in domains with frequent ultramafic outcrops (c) of 4 km [*Escartin and Cannat*, 1999].

For the well-mapped SWIR region between 61° and 66°E, the estimated regional proportion (E) of mantle-derived ultramafics in the oceanic crust is 32%, for an areal proportion of domains with frequent ultramafic outcrops (A) of 41%, a magmatic component (m) of only 10% in these domains, a mean regional seismic crustal thickness (C) of 3.5 km [*Minshull*

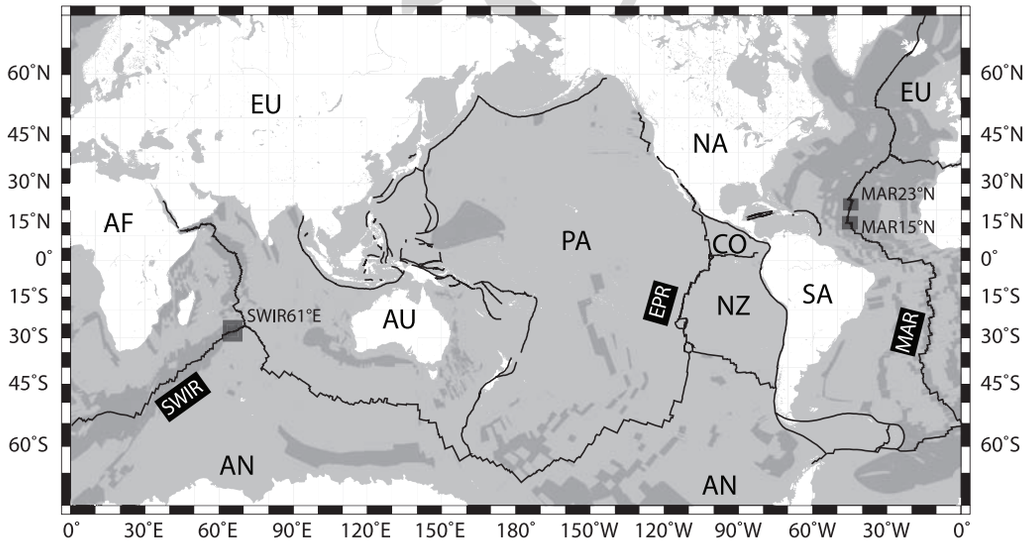

Figure 4. World map based on the study by *Bird* [2003], showing seafloor formed at spreading rates <40 mm a^{-1} in a darker shade of gray. This includes about 50% of the total length of present-day ridges and about 23% of the total surface of oceanic domains. The three type regions discussed in text (MAR 23° and 15°N, and SWIR 61°E) are shown as dark gray boxes. Abbreviations are as follows: AF, African Plate; EU, European Plate; AU, Australia plate; AN, Antarctic plate; PA, Pacific plate; NZ, Nazca plate; NA, North American plate; SA, South American plate.

et al., 2006; *Muller et al.*, 1999], and a mean gravity-derived crustal thickness in domains with frequent ultramafic outcrops (*c*) of 3 km [*Cannat et al.*, 2003].

We view the value of *E* estimated for the 23°N MAR region (9%) as a conservative estimate for the most general case of slow and ultraslow ridges that have a regional melt supply near the global average (equivalent to a 6- to 7-km-thick magmatic crust) [*Chen*, 1992]. Melt-poor environments such as our other two key areas (MAR 15°N and SWIR 61-69°E) have greater estimated *E* values (20–30%), but are not as common, and their additional contribution may be counterbalanced by near hot spot ridge regions, with a higher than normal melt supply, which do not expose ultramafics.

Using the plate boundaries database of [*Bird*, 2003], we now calculate that ridges slower than 40 mm a^{-1} represent a total length of 31,880 km, back-arc basins excluded, with an average spreading rate of 22.8 ± 8 mm a^{-1} (Figure 4). The annual rate of crustal production for these slow ridges is about 0.72 km^2 a^{-1} in surface or 4.3 km^3 a^{-1} for an average crustal thickness of 6 km. Domains with frequent outcrops of ultramafic rocks, which we infer represent $A = 23\%$ of the new seafloor formed at slow spreading ridges, could therefore represent about 0.16 km^2 of new seafloor every year. We view this estimate as relatively robust because *A* is reasonably well constrained using the gravity and seafloor morphology proxies (see section 2.1). We then estimate that the newly accreted ultramafic crustal component is about 0.39 km^3 a^{-1} ($E = 9\%$ of 4.3 km^3 a^{-1}). We view this estimate as less robust, primarily because *m* is more difficult to constrain from field data. Note that, while slow ridges represent a little over 50% of the total length of present day ridges, seafloor, which formed at rates ≤40 mm a^{-1}, represents only about 23% of the total oceanic surface (Figure 4).

Because mantle exhumation occurs by asymmetric detachment faulting (Figure 3), ultramafic rocks are emplaced only in one plate at a given time and location. Assuming that exhumation rates are equal to the half spreading rate, which would be the case for the longer-lasting detachments [*Buck et al.*, 2005], to produce 23% of the total surface of newly created crust would mobilize 46% of the total length of slow spreading ridges or 14,660 km.

3. WHAT IS THE DEGREE OF SERPENTINIZATION IN THE CRUST OF DOMAINS WITH FREQUENT ULTRAMAFIC OUTCROPS?

Increasing serpentinization of peridotites results in a linear decrease of both seismic velocity and density, from nearly 8 km s^{-1} and 3300 kg m^{-3} at zero serpentinization, to 5 km s^{-1} and 2500 kg m^{-3} at 100% serpentinization [*Christensen*, 1966, 1972; *Horen et al.*, 1996; *Miller and Christensen*, 1997]. Seismic velocity models can therefore be used to infer the degree of serpentinization, and its evolution with depth, in the crust of domains with frequent ultramafic outcrops. This is shown in Figure 5 for the location of ODP site 920, in the MAR 23°N region.

There are three principal limitations, however, to the use of this seismic velocity proxy: (1) low Vp in the upper oceanic crust also results from increased porosity and fracturation [*Detrick et al.*, 1994; *Spudich and Orcutt*, 1980]. This appears to be the case in the upper 1 to 1.5 km of domains with frequent ultramafic outcrops, which commonly have modeled Vp <5 km s^{-1} (Figures 5b and 5c), and may therefore not be interpreted directly in terms of degrees of serpentinization; (2) the proportion (*m*) of gabbros in the crust of domains with frequent ultramafic outcrops is poorly constrained. The Vp range for gabbro (6.7 to 7.3 km s^{-1} for gabbros drilled in the MAR 23°N region) [*Miller and Christensen*, 1997] is similar to that of 20% to 45% serpentinized peridotites. Greater values of *m* for a given seismic velocity-depth profile, therefore, result in larger estimated degrees of serpentinization in the upper crust and lower degrees in the deep crust (Figure 5d); and (3) seismic velocity models are not resolved beyond a few hundred meters, so that homogeneous and moderate serpentinization would have the same seismic signature over that scale, as inhomogeneous, and locally much higher, serpentinization (Figure 6).

These limitations can be somewhat overcome using geological information. The drill core at site ODP 920 in the MAR 23°N region is the longest available section of exhumed ultramafics at a slow spreading ridge. It is 200 m long and has an average degree of serpentinization of 86 ± 16% (based on thin section descriptions) [*Shipboard Scientific Party*, 1995]. Since mantle-derived peridotites emplaced near the seafloor have been exhumed tectonically from deeper levels (Figure 3), we infer that their degree of serpentinization represents a maximum for the underlying crustal section. This assumption does not necessarily hold, however, if serpentinization of the exhumed mantle is not a steady state process.

Serpentinization within the core at site ODP 920 varies at centimeter, decimeter, and decameter scale [*Dilek et al.*, 1997; *Shipboard Scientific Party*, 1995], so that the homogeneous serpentinization end-member shown in Figure 6a is clearly not applicable. The heterogeneous serpentinization end-member in Figure 6b is not valid either, however, because unserpentinized peridotites have not been recovered (the least altered samples at site 920 are about 40% serpentinized) [*Miller and Christensen*, 1997]. An intermediate configuration, between the two sketched in Figure 6, is therefore the most likely.

Figure 5d shows the range of variation of the estimated degree of serpentinization with depth in the ultramafic com-

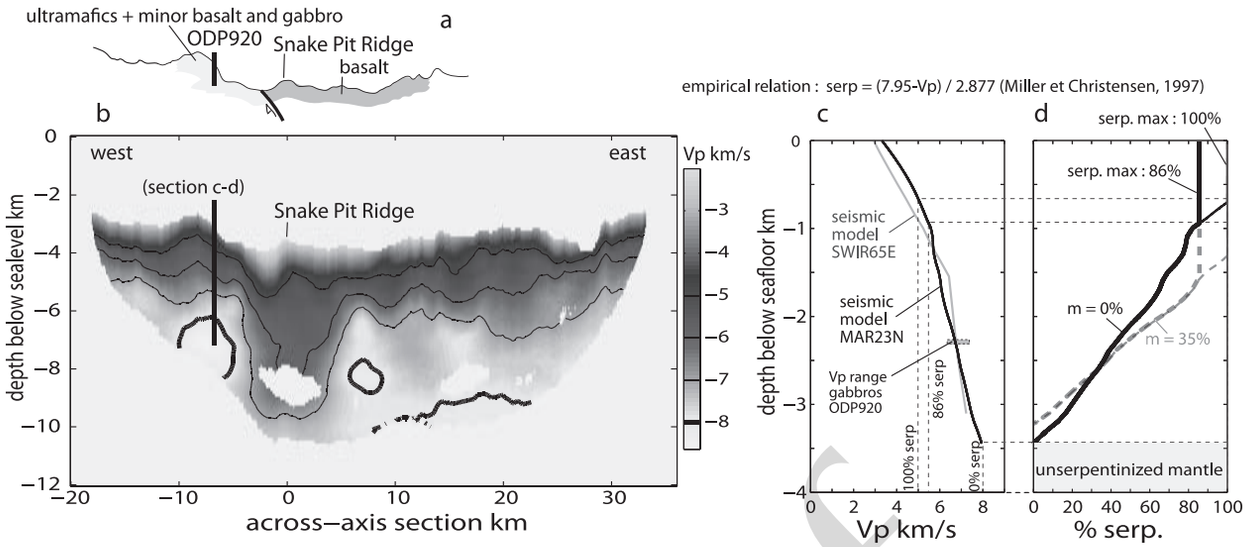

Figure 5. (a) Seafloor tomography. (b and c) The seismic velocity structure of ultramafic-bearing crust of the 23°N MAR region [*Canales et al.*, 2000], and (d) its interpretation in terms of degree of serpentinization. This seismic section is located in Figure 2. It goes over ODP Site 920 [*Shipboard Scientific Party*, 1995], and the vertical profile in Figure 5c corresponds to this location. Seafloor topography in the simplified geological section in Figure 5a is drawn at the same scale as the seismic section in Figure 5b. Percent serpentinization in Figure 5d is the maximum calculated value (see text) for four settings: exhumed ultramafics with a maximum degree of serpentinization of 86% or 100%, and with no gabbros, or 35% gabbros (in volume).

ponent of the crust, for two values of the gabbroic component (0% and 35%), and two values (86% and 100%) of the maximum degree of serpentinization (Figure 6). These curves correspond to average degrees of serpentinization of the ultramafic component of the crust ranging between 57% (86% maximum serpentinization, no gabbros in the crust) and 72% (100% maximum serpentinization, 35% of gabbros in the crust).

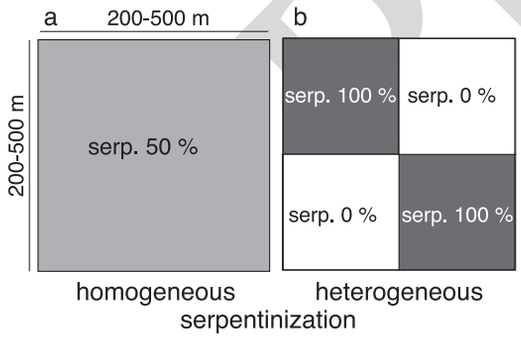

Figure 6. Seismic velocity models do not resolve beyond a few hundred meters. This sketch shows two end-member serpentinization patterns, which would have similar seismic velocity signatures: (a) homogeneously distributed serpentinization and (b) very heterogeneous serpentinization, with domains of fresh peridotites juxtaposed with highly serpentinized domains. These two end-member serpentinization patterns should result in highly contrasted hydrogen fluxes, for the same overall average degree of serpentinization.

4. ESTIMATING HYDROGEN AND METHANE FLUXES ASSOCIATED WITH SERPENTINIZATION

Magnetite forms to incorporate the iron released during the serpentinization of olivine [*Frost*, 1985; *Moody*, 1976]. Reaction (1), shown below, corresponds to the end-member case in which all the iron goes into magnetite. Dissociation of water during magnetite crystallization forms 1 mol H_2 for each mole of magnetite. A portion of the hydrogen produced may then combine with dissolved CO_2, to form methane (reaction (2)). Magnetite may act as a catalyst for this Fischer-Tropsch type reaction [*Berndt et al.*, 1996].

$$2\,Mg_{1.8}Fe_{0.2}SiO_4 + 2.73\,H_2O = Mg_3Si_2O_5(OH)_4 + 0.6\,Mg(OH)_2 + 0.133\,Fe_3O_4 + 0.133\,H_2 \quad \text{(R1)}$$

$$CO_2 + 4\,H_2 = CH_4 + 2\,H_2O \quad \text{(R2)}$$

4.1. Estimating Hydrogen Fluxes per Kilometer of Ridge Axis From the Proportion of Serpentine in Slow Spreading Crust

Reaction (1) corresponds to the crystallization of iron-free serpentine and brucite. However, petrological studies have shown that the serpentinization of abyssal and ophiolitic peridotites is a complex process, involving the crystallization of iron-rich serpentine and small amounts of magnetite in the early stages, then, as serpentinization proceeds, of iron-poor serpentine and more magnetite [*Oufi et al.*, 2002; *Toft et al.*, 1990; *Wicks and O'Hanley*, 1988]. This results in a strongly nonlinear increase of magnetite content (and associated hydrogen release), as serpentinization proceeds (Figure 7). This nonlinearity is best documented in studies of the magnetic susceptibility of ophiolitic samples [*Toft et al.*, 1990], and of drilled abyssal samples [*Oufi et al.*, 2002]. The initial magnetite susceptibility per unit volume can be approximated as a linear function of the magnetite volume percent [*Toft et al.*, 1990]. Using this approximation, it becomes possible to show that the magnetite content of serpentinized peridotites increases dramatically for degrees of serpentinization >70% (Figure 7a). Although this strong increase is recorded in all sample sets, there is a significant scattering (partly due to the size of the measured samples, which is commonly too small to adequately represent the mineralogy) and a variability between sample sets (Figure 7a). This variability is best exemplified by the lower magnetite contents in drilled serpentinized peridotites from ODP site 1274, in the MAR 15°N region. Samples from this ODP site, which have been more than 70% serpentinized, contain less magnetite than most similarly altered samples in other drill cores [*Bach et al.*, 2004, 2006].

Two empirical exponential relations have been proposed by [*Oufi et al.*, 2002] to fit magnetite content to the degree of serpentinization in abyssal sample sets. Curve a approximates the scatter in most abyssal samples, and curve b fits the ODP site 1274 sample set (Figure 7a). The interpretation of these magnetite production curves in terms of a suite of serpentinization reactions (Figure 7b) is based on observations made by *Oufi et al.* [2002] and *Bach et al.* [2006] on ODP drilled samples. A larger set of reactions may be activated, however, and result in other magnetite production curves [*Toft et al.*, 1990]. Specifically, it is possible to obtain low magnetite production rates during serpentinization with substantial iron dissolution in the hydrothermal fluid. This may, for example, account for the high dissolved iron content of hydrothermal fluids at the R and L vents (Table 1). Crystallization of Fe^{3+}-bearing serpentine in the early stages of serpentinization may also release hydrogen in addition to that produced during magnetite formation [*Seyfried et al.*, 2007]. In the calculations presented in this chapter,

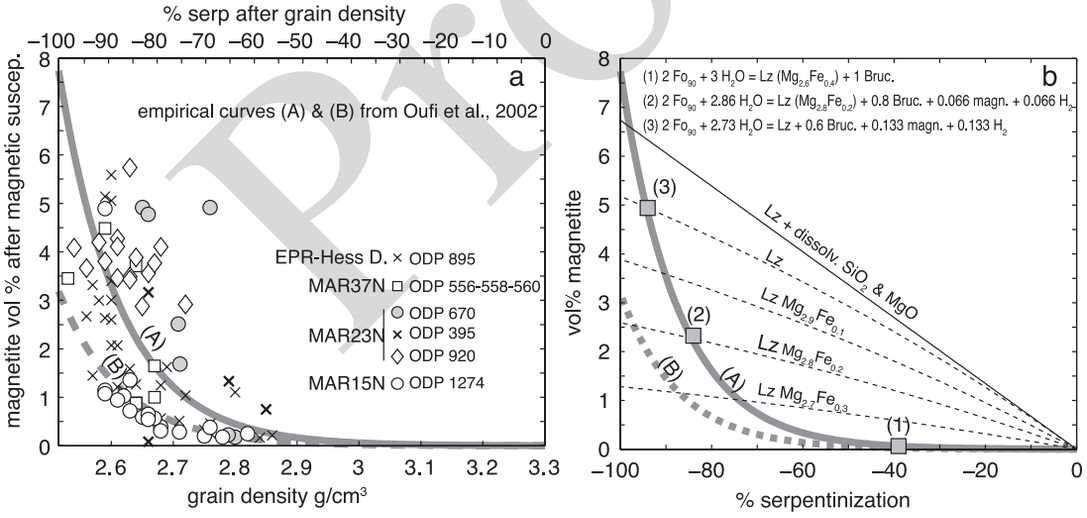

Figure 7. Production of magnetite and hydrogen as a function of the degree of serpentinization in abyssal peridotites. (a) Abyssal peridotites drilled at near-ridge locations in the Atlantic (all ODP sites but 895) and Pacific (ODP 895, Hess Deep). Modified after the study of *Oufi et al.* [2002], including new data from ODP Site 1274 [*Bach et al.*, 2006]. Magnetite content is inferred from magnetic susceptibility, and percent serpentinization is inferred from grain density. Details and references in text. Empirical magnetite production curves a and b are drawn to fit the characteristics of abyssal samples. (b) These empirical curves can be reproduced with a succession of serpentinization reactions, which produce progressively more iron-poor serpentine [*Toft et al.*, 1990; *Oufi et al.*, 2002].

Table 1. Hydrogen, Methane, CO_2, and Dissolved Iron Concentrations in Fluids From Three Ultramafic-Hosted Systems of the Mid-Atlantic Ridge (MAR) and Corresponding Fluxes Estimated for the Rainbow (R) Hydrothermal Field[a]

	H_2, mmol kg^{-1}	CH_4, mmol kg^{-1}	CO_2, mmol kg^{-1}	Fe, μmol kg^{-1}	QH_2, 10^7 mol a^{-1}	QCH_4, 10^7 mol a^{-1}	QH_2 Initial[b], 10^7 mol a^{-1}	QFe_{diss}, 10^7 mol a^{-1}
R (365°C/2300 m) [*Charlou et al.*, 2002]	16	2.5	16	24,000	24 ± 11	3.9 ± 1.7	39 ± 17	37 ± 16
Logatchev (L; 350°C/3000 m) [*Charlou et al.*, 2002]	12	2.1	10.1	2,500	–	–	–	–
Lost City (LC; 50–90°C/750 m) [*Kelley et al.*, 2005]	0.5–15	1–2	$<10^{-3}$	<<	–	–	–	–

[a]See section 4.3.
[b]Prior to methane production (reaction (2)).

we ignore hydrogen production due to Fe^{3+} in phases other than magnetite.

In Figure 8, we use magnetite production curves a and b to predict the magnetite and hydrogen production associated with serpentinization in domains of frequent ultramafic outcrops. In Figure 9, we show the integrated hydrogen fluxes calculated from each depth section in Figure 8, per year, per kilometer of axis (in domain with frequent ultramafic outcrops), and for an exhumation rate of 10 mm a^{-1}. In order to calculate these fluxes, we assume that serpentinization occurs in a steady state fashion, as plates move apart and as mantle exhumation proceeds at the ridge axis (Figure 3). At the exhumation rate of 10 mm a^{-1}, we calculate that this steady state serpentinization consumes between 11.3 m^3 (35% gabbros and maximum serpentinization equal to 86%) and 17.6 m^3 (no gabbros and maximum serpentinization equal to 100%) of fresh peridotite per year and per kilometer of axis. The first value (11.3 m^3) corresponds, for the average exhumation rate of 11.4 mm a^{-1}, and over the 14,660 km of slow spreading ridges where exhumation is inferred to occur, to an annual global consumption of 0.18 km^3 of fresh peridotites. With a volume increase of 30% during serpentinization, this corresponds to the annual production of 0.23 km^3 of serpentine, or 6% of the estimated crustal production at ridges slower than 40 mm a^{-1}. This 6% estimate is in excellent agreement with the 5% value proposed by *Carlson* [2001], using a different method, for the serpentine component in MAR crust.

As will be discussed later, the steady state serpentinization assumption is not necessarily valid. The hydrogen fluxes in Figure 9 may, nonetheless, be used as time and/or space-integrated values to predict fluxes over lengths of time, and/or lengths of ridge, greater than the period and/or scale of variability of the serpentinization process.

Figures 8 and 9 distinguish 16 different contexts, which we propose cover the possible range of magnetite production in serpentinized exhumed mantle at slow and ultraslow ridges. These 16 contexts result from various combinations of four principal parameters: the maximum degree of serpentinization (calculations made for 86% and 100%; Figure 5d), the homogeneous or heterogeneous distribution of serpentinization (calculations made for the two end-members shown in Figure 6), the proportion of gabbros in the exhumed ultramafics (calculations made for 0% and 35%), and the rate of magnetite production during serpentinization (calculations made for curve a or curve b in Figure 7). The uncertainties attached to the estimated hydrogen fluxes in Figure 9 primarily arise from lack of geological constraints: Is the proportion of gabbros closer to 0% or 35%, is serpentinization dominantly heterogeneous or homogeneous, and what is the magnetite and hydrogen production rate? The order of magnitude of these uncertainties may be assessed from the range of possible H_2 flux estimates in Figure 9. These estimated fluxes vary over more than one order of magnitude, ranging between 0.288 10^7 mol a^{-1} km^{-1} (35% gabbros, maximum serpentinization equal to 86%, curve b, and homogeneous serpentinization) and 3.61 10^7 mol a^{-1} km^{-1} (0% gabbros, maximum serpentinization equal to 100%, curve a, and heterogeneous serpentinization). Based on available samples (see discussion in section 3), we view the 100% maximum serpentinization configuration as not the most likely scenario. It does, however, provide useful estimates for the maximum possible time and/or space-integrated hydrogen fluxes (Figure 9). Sample studies also indicate that reality is probably somewhere in between the strictly homogeneous and the strictly heterogeneous serpentinization configurations of Figure 6. This would correspond to hydrogen fluxes of the order of 10^7 mol a^{-1} km^{-1}, for an exhumation rate of 10 mm a^{-1} (Figure 9).

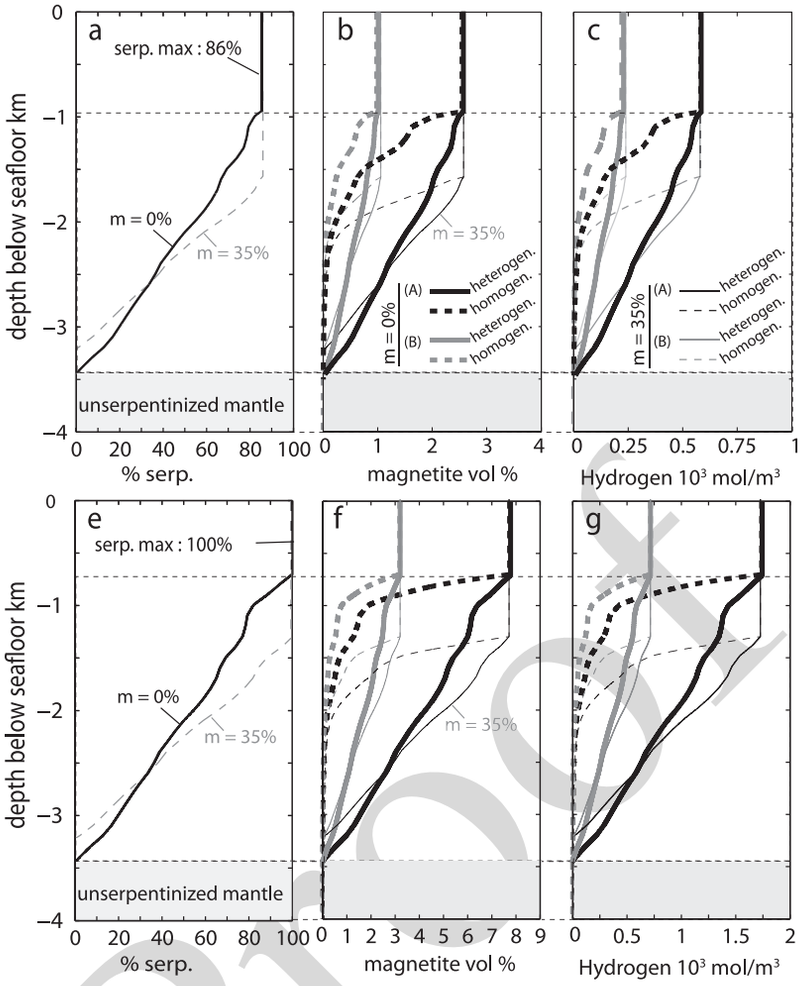

Figure 8. Production of magnetite and hydrogen calculated from the serpentinization profiles derived in Figure 5d, using the empirical magnetite production curves a and b (Figure 7). Sixteen different configurations are explored: 0% or 35% gabbros, maximum serpentinization equal to 86% or 100%, strictly homogeneous or strictly heterogeneous serpentinization (Figure 6), magnetite production curve a or b.

4.2. Estimating Hydrogen and Methane Fluxes From Regional Hydrothermal Heat Loss

Recent studies at the MAR have shown that a substantial part of the serpentinization there is linked with high temperature, black smoker-type hydrothermal cells, which are fuelled primarily by magmatic heat [*Allen and Seyfried*, 2004; *Lowell*, 2007; *Seyfried et al.*, 2004]. Large volumes of peridotites are also involved in serpentinization reactions associated with lower temperature vents, such as the LC field [*Kelley et al.*, 2001], which may [*Allen and Seyfried*, 2004] or may not [*Fruh-Green et al.*, 2003] also be at least partially fuelled by magmatic heat. Whatever the case, these vents collectively extract a significant part of the total heat released by the ridge. In this section, we use estimates of this total hydrothermal heat flux, and the ratios of hydrogen and methane concentrations in the hydrothermal fluids (Table 1) to the vent's heat output (equation (2)), to estimate serpentinization-related hydrogen and methane fluxes per kilometer of ridge axis (equation (3)).

The two ultramafic-hosted black smoker fields selected for this study (R and L) yield similar H_2/heat and CH_4/heat ratios (Table 2). The variability of vent fluid temperature and composition is greater at LC. Consequently, the calculated H_2/heat and CH_4/heat ratios there are up to 10 times larger than at the other two sites (Table 2). The dissolved iron to heat ratios can also be calculated in the same way and differ dramatically between the three hydrothermal fields (Table 2).

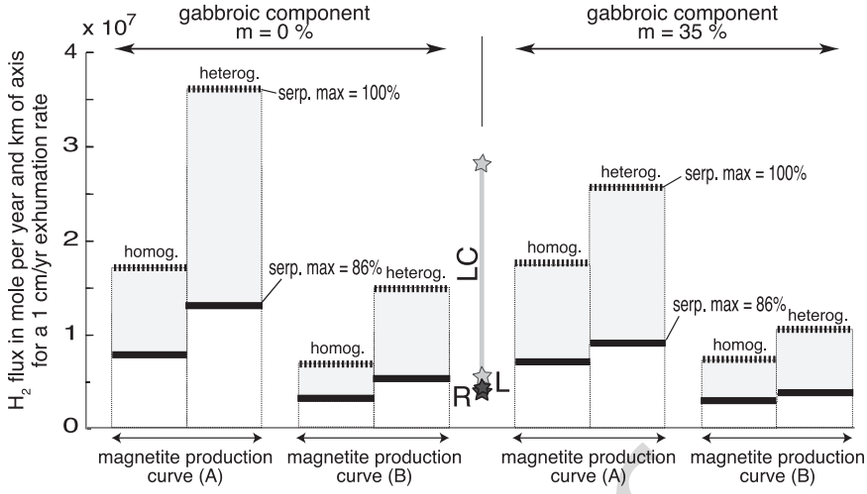

Figure 9. Hydrogen fluxes calculated for domains of exhumed ultramafics, per kilometer of ridge axis and for an exhumation rate of 1 cm a^{-1}. These fluxes are calculated from each of the 16 hydrogen production profiles in Figures 8c and 8g, for steady state serpentinization of a volume corresponding to a unit length of the ridge axis, multiplied by the thickness of the crustal layer, multiplied by the exhumation rate minus the proportion of gabbros (*m*). Estimated fluxes for maximum serpentinization equal to 86% are shown as thick black lines, and to 100% as thick dashed lines. Estimates for strictly homogeneous or strictly heterogeneous serpentinization (Figure 6) are juxtaposed. To estimate hydrogen fluxes at a different exhumation rate, simply multiply value in Figure 9 by the inferred exhumation rate in the region of interest. Independent estimates based on axial hydrothermal heat fluxes and on hydrogen concentrations in fluids from the Rainbow (R), Logachev, and Lost City vents are shown as stars. These values (between parentheses in Table 2) were calculated for an exhumation rate equal to the half spreading rate and would be lower for a faster inferred exhumation rate.

$$H_2 / \text{heat} = cH_2 / (cpT), \qquad (2)$$

where T is the fluid temperature, cH_2 the hydrogen concentration, and cp the fluid heat capacity.

The total heat extracted at mid-ocean ridges can be estimated from heat flow measurements [*Stein and Stein*, 1994] and from numerical models of the ridge's thermal regime [*Chen and Phipps Morgan*, 1996; *Pelayo et al.*, 1994], which use geophysical observations to constrain the depth of isotherms [*Chen and Morgan*, 1990]: the depth to the brittle-ductile transition temperature (~750°C) [*Hirth et al.*, 1998] is approximated from the maximum depth of seismicity [*Barclay et al.*, 2001; *Toomey et al.*, 1988; *Wolfe et al.*, 1995], while the depth to magmatic temperatures (≥1100°C) is inferred from the depth to a melt lens imaged by seismic reflection and refraction data [*Collier and Sinha*, 1990; *Detrick et al.*, 1987; *Kent et al.*, 1993]. The greatest part of this heat is extracted through hydrothermal systems (the ra-

Table 2. Ratio of Hydrogen, Methane, and Dissolved Iron Concentrations to Heat in Fluids From Three Ultramafic-Hosted Systems of the MAR, With Corresponding Fluxes (Q) Estimated for Ridge Domains With Frequent Ultramafic Outcrops, From the Estimate of Total Hydrothermal Heat Flux[a]

	H_2/heat, 10^{-9} mol J^{-1}	CH_4/heat, 10^{-9} mol J^{-1}	Fe_{diss}/heat, 10^{-9} mol J^{-1}	QH_2heat, 10^7 mol a^{-1} km^{-1}	QCH_4heat, 10^7 mol a^{-1} km^{-1}	QH_2heat Initial[b], 10^7 mol a^{-1} km	QFe_{diss}heat, 10^7 mol a^{-1} km^{-1}
R (365°C/2300 m)	5.15	0.8	7.73	0.26	0.04	0.42 (0.37)	0.39
L (350°C/3000 m)	5.8	1	1.2	0.29	0.05	0.49 (0.43)	0.06
LC (50–90°C/750 m)	1.4–41[c]	2.7–5.5[c]	<<	0.07–2.08[c]	0.14–0.28[c]	0.62–3.2[c] (0.54–2.8)[c]	<<

Q4 [a]See Table 1 and section 4.2. Values in parentheses are calculated from an inferred exhumation rate of 11.4 mm a^{-1} (equal to the half spreading rate at R) back to an exhumation rate of 10 mm a^{-1}.

[b]Prior to methane production (reaction (2)).

[c]For a fluid temperature of 90°C.

tio of hydrothermal to conductive heat flux deduced from thermal models at mid-ocean ridges is typically greater than 8) [*Phipps Morgan et al.*, 1987]. Simple analytical solutions have been proposed to calculate this total heat flux, which take into account the heat supplied by magma and by cooling of the axial lithosphere to specified, geophysically constrained, thermal configurations [*Baker*, 2007; *Cannat et al.*, 2004; *Mottl*, 2003]. Here we use the equations and constants given by *Cannat et al.* [2004], with a magma supply equivalent to a 6-km-thick magmatic crust, cooling of the lower crust to an average temperature of 400°C on axis, and with a root of axial mantle lithosphere which is cooled to an average temperature of 700°C down to 8 km below seafloor.

For a spreading rate of 22.8 mm a^{-1}, which corresponds to the average spreading rate for ridges slower than 40 mm a^{-1} (Figure 4; see section 2.3), this corresponds to a heat flux of 19 MW km^{-1}. This is about 3 MW km^{-1} more than the value calculated by *Baker* [2007] for the same spreading rate. The difference is due to cooling of the mantle lithosphere, which is not taken into account by *Baker* [2007]. In the following calculations, we will use a conservative value of 16 MW km^{-1} for the hydrothermally released heat flux (Heat in equation (3)) at our average spreading rate (22.8 mm a^{-1}) slow ridge. This is equivalent to assuming that the difference between Baker's and our estimate of total heat flux corresponds to the conductive heat flux component.

Ridge segment centers receive more melt, while the thickness of cooled mantle is greater at segment ends. As shown by *Cannat et al.* [2004], the total hydrothermal heat flux per kilometer of ridge probably thus does not vary by more than a few units between magma-rich segment centers and domains with frequent ultramafic outcrops at segment ends. Serpentinization releases additional heat. We calculated this serpentinization-related heat flux for the four different serpentinization versus depth curves shown in Figure 5d, using a heat of reaction of 0.25 MJ kg^{-1} [*Fyfe*, 1974] and found it to be relatively minor (0.33 to 0.5 MW km^{-1} for an exhumation rate equal to the half spreading rate of 11.4 mm a^{-1}).

We now use our estimate of the hydrothermal heat flux per kilometer of ridge (Heat), and the H_2/heat, CH_4/heat, and Fe_{diss}/heat ratios calculated for the R, L, and LC vent fields (Table 2), to derive serpentinization-related hydrogen and methane fluxes per kilometer of ridge axis (equation (3)). We therefore make the hypothesis that serpentinization-related fluids at slow ridges are primarily released into the water column via R-L- or LC-type hydrothermal vents. The possibility exists, however, that serpentinization-derived fluids also exit in a more diffuse fashion, with different and as yet unconstrained H_2/heat, CH_4/heat, and Fe_{diss}/heat ratios. In addition, we use the hydrogen and methane content of the fluids as they exit the vents, and these may have been modified by subsurface biological interactions. Finally, our calculation assumes a steady state hydrothermal heat flux, which is probably not the case [*Humphris and Cann*, 2000; *Wilcock and Delaney*, 1996]. Similarly to the hydrogen fluxes, which we estimated independently in section 4.1 (Figure 9), equation (3) therefore provides estimates of time and/or space-integrated fluxes, over lengths of time, and/or lengths of ridge, greater than the period and/or scale of variability of hydrothermal circulations.

$$QH_2\text{heat} = \text{Heat } H_2 \text{ / heat in mol km}^{-1}. \quad (3)$$

We perform the calculation for a ridge that spreads at the average slow rate of 22.8 mm a^{-1} (which incidentally is close to the spreading rates at the three hydrothermal sites used in this study) [*DeMets et al.*, 1994]. The results are listed in Table 2. QH_2heat and QCH_4heat values show a good homogeneity for the two black smoker sites (R and L), as could be predicted from the H_2/heat and CH_4/heat values, and a large variability in the case of LC. The uncertainties attached to these QH_2heat and QCH_4heat flux values are partially associated with uncertainties in the estimated hydrothermal heat loss, which we propose could be of the order of 20% (16 ±3 MW km^{-1}). However, as for the hydrogen fluxes estimated in section 4.1 (Figure 9), the largest uncertainties are attached to a lack of geological, and in this case, also biological constraints: Is the ridge primarily cooled through high temperature and focused hydrothermal vents or through more diffuse circulations, and what is the hydrogen and methane consumption of the subseafloor biosphere?

In order to compare the QH_2heat and QCH_4heat estimated flux values in Table 2, with the prediction based on the estimated proportion of serpentine in slow spreading crust (Figure 9), we must first recombine QCH_4heat into the equivalent hydrogen flux (4 mol H_2 for 1 mol CH_4; reaction (2)). This gives a total initial (prior to reaction (2)) hydrogen flux (QH_2heat initial). We make the hypothesis that exhumation of mantle-derived rocks that are being serpentinized occurs at a rate equal to the half spreading rate or 11.4 mm a^{-1}. After a rule of thumb correction to an exhumation rate of 10 mm a^{-1}, the QH_2heat initial values in Table 2 are seen to cover the same range as the hydrogen fluxes calculated independently from the serpentinization versus depth curves of Figures 5 and 8 (Figure 9). QH_2heat initial values estimated for R, L, and the lower estimate for LC plot at the lowermost range of these calculated flux values (Figure 9). The higher QH_2heat initial value estimated for LC, which are obtained for the hydrogen-rich fluid end-member (Table 1), would correspond to higher maximum serpentinization rates and to the high magnetite-production curve a.

In the case of R and L, the high concentrations of dissolved iron in the fluids (Table 1) could indicate that less magnetite and hydrogen was produced per kilometer of ridge (3 mol dissolved iron for 1 mol magnetite and 1 mol hydrogen; reaction (1)), than predicted in section 4.1 using magnetite production curves a and b. The flux of dissolved iron at these vents would then require serpentinization of an additional volume of fresh peridotite. The interpretation of the magnetite production curves used in section 2.1 in terms of a suite of serpentinization reactions (Figure 7b) is, however, based on a small number of detailed petrographic studies (see Figure 7 caption), and it is, in theory, possible to obtain low magnetite production rates similar to curve b with a different set of reactions, involving the formation of less iron-rich serpentine and substantial iron dissolution. Petrographic studies of ultramafics from the R or L basement are therefore required to pursue this discussion.

4.3. Hydrogen and Methane Fluxes at the Ultramafic-Hosted Rainbow Hydrothermal Vent Field: How Do They Fit With Estimated Hydrogen Fluxes per Kilometer of Ridge Axis?

The R field is a 100 m by 200 m area of ultramafic-hosted black smokers, set in the footwall of the eastern axial valley bounding fault, at the northern end of the short South AMAR ridge segment (Plate 1). The vent fluids are hot (365°C) and have high hydrogen, methane, and dissolved iron concentrations (Table 1), which are attributed to serpentinization [*Charlou et al.*, 2002]. Detailed physical oceanography data are available, showing that the hydrothermal plume is advected to the northeast as a single coherent structure, toward the rift valley of the AMAR segment [*German et al.*, 1998]. These hydrographic conditions are exceptionally adapted to the use of helium isotopic concentrations to trace plume dispersion and to calculate hydrothermal fluxes [*Jean-Baptiste et al.*, 2004]. We do not yet have equivalent data to quantify fluxes at other ultramafic-hosted vent fields such as L or LC.

The flux of ^{3}He in the R plume has been used by *Jean Baptiste et al.* [2004] to derive the integrated fluid flux (Qf = 490 ± 220 kg s^{-1}) of the R field. This calculated fluid flux value can be used, knowing the hydrogen (cH_2) and methane (cCH_4) concentration in the hydrothermal fluid (Table 1), to derive the integrated hydrogen ($QH_2 = Qf.cH_2 = 7.8 \pm 3.5$ mol s^{-1} or $24 \pm 11\ 10^7$ mol a^{-1}) and methane ($QCH_4 = Qf.cCH_4 = 1.2 \pm 0.5$ mol s^{-1} or $3.9 \pm 1.7\ 10^7$ mol a^{-1}) fluxes (Table 1). A flux of dissolved iron ($QFe = Qf.cFe = 11.8 \pm 5.2$ mol s^{-1} or $37 \pm 16\ 10^7$ mol a^{-1}) can also be calculated.

In order to compare these values, with the prediction based on the estimated proportion of serpentine in slow spreading

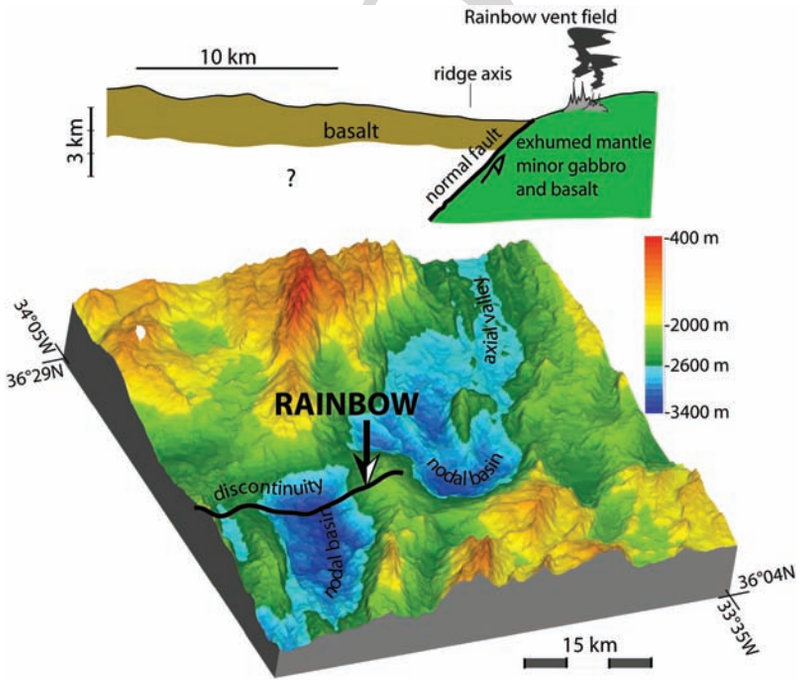

Plate 1. Setting of the R vents (arrow) in the nontransform offset between the AMAR and the south AMAR segments of the MAR [*Gràcia et al.*, 2000]. Block diagram from bathymetric data given by *Cannat et al.* [1999a]. Geological setting is summarized in simplified section.

crust (Figure 9), we first recombine QCH_4 into the equivalent hydrogen flux (4 mol H_2 for 1 mol CH_4; reaction (2)). This gives a total initial (prior to reaction (2)) hydrogen flux for R QH_2 initial = $39 \pm 17\ 10^7$ mol a^{-1}. The total spreading rate at R is about 2.3 cm a^{-1} [*Demets et al.*, 1994]. Assuming that detachment faulting and exhumation at R occur at a rate equal to the half spreading rate, the highest predicted hydrogen flux at this spreading rate (for the unlikely end-member case of 0% gabbros, maximum serpentinization equal to 100%, magnetite production curve a, and strictly heterogeneous serpentinization; Figure 9) is 4.1×10^7 mol a^{-1} km^{-1} ($[1.15 \times 3.61] \times 10^7$ mol a^{-1} km^{-1}). The lowest predicted hydrogen flux (for the less unlikely end-member case of 35% gabbros, maximum serpentinization equal to 86%, magnetite production curve b, and strictly homogeneous serpentinization; Figure 9) is 0.33×10^7 mol a^{-1} km^{-1} ($[1.15 \times 0.288] \times 10^7$ mol a^{-1} km^{-1}). With these end-member values, QH_2 initial estimated for the R field is equivalent to the hydrogen flux calculated for a steady state serpentinization process occurring over a ridge length of 9.4 to 118 km. With the independently estimated QH_2heat initial value at R (Table 2), the requirement would be for steady state serpentinization occurring over a ridge length of 105 km. This seems unrealistically long, given that the along-axis length of domains with frequent ultramafic outcrops surrounding the R field in the AMAR and South AMAR segments (Plate 1) is probably <50 km.

Furthermore, the additional production of $37 \pm 16 \times 10^7$ mol a^{-1} dissolved iron is equivalent to a deficit of $12.3 \pm 5 \times 10^7$ mol a^{-1} in magnetite and hydrogen production (3 mol dissolved iron for 1 mol magnetite and 1 mol hydrogen). This flux of dissolved iron may thus require (see discussion in section 4.2) the serpentinization of an additional volume of fresh peridotite, equivalent to adding 3 to 58 km to the estimated ridge length over which steady state serpentinization should occur to feed the R vents.

5. DISCUSSION

We have proposed two sets of estimates for the hydrogen flux related to serpentinization at slow spreading ridges. One set of estimates was obtained based on serpentinization versus depth profiles calculated from seismic data for the crust of domains with frequent ultramafic outcrops (Figure 5). The other set of hydrogen flux values was calculated based on estimated axial hydrothermal heat fluxes, assuming that in domains with frequent ultramafic outcrops heat is primarily expelled by hydrothermal fluids similar to those of known ultramafic-hosted vent fields. It is worth noting that, although the hydrogen fluxes estimated with each method vary over about one order of magnitude, the ranges of values derived by the two methods overlap (Figure 9). This means that no contradiction is apparent at this point, between hydrogen fluxes estimated from axial cooling by hydrothermal fluids, which would have the composition of known ultramafic-hosted vent fluids and the estimated rates at which fresh peridotite may be serpentinized in the underlying basement.

It is also necessary to note that the serpentinization versus depth profiles provide an estimate of the total serpentinization undergone by the ultramafic component of the crust, as it leaves the axial domain. The first method therefore does not resolve the effect of multiple episodes of serpentinization [*Andreani et al.*, 2007], possibly with variable reaction rates. The other method uses an estimate of total hydrothermal heat flux which is calculated for a steady state melt supply and for a steady state geometry of isotherms at the ridge axis. It therefore does not resolve the possible effect on serpentinization of short-scale variations in melt supply and in the vigor of hydrothermal convection [*Wilcock and Delaney*, 1996]. Both methods therefore provide flux values, which should be considered as averages over about the age of the axial domain (700 ka to 1 Ma).

The first method is strongly dependent on the degree of serpentinization, on the behavior of iron as serpentinization proceeds, and to a lesser extent, on the proportion (m) of magmatic rocks in sections of exhumed and altered mantle. Based on available drilling and surface geology data, we have argued (section 4.1) that this first method suggests serpentinization-related hydrogen fluxes of the order of 10^7 mol a^{-1} km^{-1}, for an exhumation rate of 10 mm a^{-1} (Figure 9). Applied to the 14,660 km of total present-day ridge length estimated to exhume ultramafics and making the hypothesis that their average exhumation rate is half of the average spreading rate (22.8 mm a^{-1}; see section 2.3), this corresponds to an estimated global serpentinization-related hydrogen flux at mid-ocean ridges of about 16.7×10^{10} mol a^{-1}. Because hydrogen has an extremely low residence time in seawater, its impact is mostly expected to be on subseafloor and very near vent ecosystems [*Kadko et al.*, 1990; *Shock and Holland*, 2004]. Part of the hydrogen produced by the serpentinization reactions, however, reacts with dissolved carbon to form methane [*Charlou and Donval*, 1993]. Experiments [*Berndt et al.*, 1996; *Foustoukos and Seyfried*, 2004; *Horita and Berndt*, 1999] indicate that methane-producing reactions occur at high temperatures (>200°C), probably within the serpentinized meshwork (because magnetite probably acts as a catalyst). Methane, having a longer residence time in the water column [*Kadko et al.*, 1990] would have a more widespread impact. Experimental constraints on the proportion of serpentinization-related hydrogen fluxes, which reacts to form methane are still few [*Berndt et al.*, 1996; *Foustoukos and Seyfried*, 2004; *Horita and Berndt*, 1999]. At this point,

it is only possible to estimate this rate from methane/hydrogen concentration ratios in fluids from ultramafic-hosted hydrothermal vents. These ratios are similar (0.15–0.17) at R and L, and for the most hydrogen-rich fluids at LC (Table 1). They would correspond to a global serpentinization-related mid-ocean ridge methane flux ($[0.15 \times 16.7] \times 10^{10}$ mol a^{-1}) of about 2.5×10^{10} mol a^{-1} (0.4 Mt a^{-1}). The minimum and maximum hydrogen fluxes estimated in Figure 9 (0.288×10^7 and 3.61×10^7 mol a^{-1} km^{-1}) would correspond to global serpentinization-related hydrogen ridge fluxes of 4.8×10^{10} and 60×10^{10} mol a^{-1} and to global methane fluxes of 0.7×10^{10} mol a^{-1} (0.1 Mt a^{-1}) and 9×10^{10} mol a^{-1} (1.4 Mt a^{-1}), respectively. *Emmanuel and Ague* [2007] propose a similarly high value (1.35 Mt a^{-1}), but use a 50% conversion rate of hydrogen to methane. *Sorokhtin et al.* [2001] propose a much higher value (9 Mt a^{-1}), but infer that serpentine forms a 2-km-thick lower crustal layer globally, yielding serpentinization rates of 5.4 km^3 a^{-1}, about 23 times higher than our preferred rate of 0.23 km^3 a^{-1}.

The second method does not require any assumption on the proportion of serpentine in the oceanic crust nor on the nature of serpentinization reactions. It does, however, strongly depend on the estimation of time-averaged axial hydrothermal heat loss, and on the composition and temperature of serpentinization-related hydrothermal circulations. It also assumes that hydrogen and methane concentrations in the hydrothermal fluid have not been modified by subseafloor biological processes. If axial hydrothermal heat loss in regions with frequent ultramafic outcrops is mostly accommodated via R- and L-type ultramafic-hosted black smoker systems, the initial hydrogen fluxes we estimate with this method are about 0.4×10^7 mol a^{-1} km^{-1} for an exhumation rate of 10 mm a^{-1} (Table 2), giving a global initial hydrogen flux of 6.6×10^{10} mol a^{-1} for present-day ridges (14,660 km and 11.4 mm a^{-1} average exhumation rate; section 2.3), of which about 15% (or 10^{10} mol a^{-1}) would react to form methane (0.16 Mt a^{-1}). Lower initial hydrogen fluxes are estimated with this second method if exhumation rates are faster, and higher initial hydrogen fluxes are estimated if axial hydrothermal heat loss in regions with frequent ultramafic outcrops is mostly accommodated via lower temperature, LC-type white smoker systems (up to 2.8 10^7 mol a^{-1} km^{-1} for an exhumation rate of 10 mm a^{-1}; Table 2). This would yield a global initial hydrogen flux of 46×10^{10} mol a^{-1} for present-day ridges, of which about 15% (or 7×10^{10} mol a^{-1}) would react to form methane (1.1 Mt a^{-1}). This is of the same order of magnitude as the estimated value of 1.6 Mt a^{-1} proposed by *Kasting and Catling* [2003], based also on methane concentrations in the LC vent fluids, with heat flux values derived from the global estimates of *Mottl and Wheat* [1994]. We focus the first part of this discussion on the pros and cons of these two hypotheses: Are serpentinization-derived fluids mostly expelled in R-type hydrothermal systems (hypothesis 1), or are serpentinization-derived fluids mostly expelled in LC-type hydrothermal systems (hypothesis 2)?

The first element of this discussion is that R- and L-type vents, with their low pH, high temperatures, and high dissolved metals and sulfur contents, undoubtedly expel significant volumes of hydrogen and methane-rich serpentinization-related fluids at the MAR. Ultramafic-hosted black smokers similar to R and L have recently been discovered at other axial valley locations [*Beltenev et al.*, 2005; *Davydov et al.*, 2007], and sulfide chimneys have been dredged next to actively forming corrugated surfaces of the 15°N area [*Beltenev et al.*, 2005; *Davydov et al.*, 2007; *Murton et al.*, 2007]. Fluids from the Saldanha ultramafic-hosted, diffuse venting area, in the MAR axial valley north of R, have not yet been sampled, but the occurrence of sulfide precipitates in the sediment next to venting pockmarks [*Dias and Barriga*, 2006] suggests that this diffuse hydrothermal area expels fluids with a higher temperature end-member more comparable to the R or L, than to the LC fluids (G. Früh-Green, personal communication, 2008).

These observations concur to indicate that R- or L-type black smokers are indeed a significant exit channel for heat- and serpentinization-derived fluids at the MAR. These vents are set on the exhumed footwall of axial detachment faults, and the composition of their fluids requires that the hydrothermal reaction zone be partly made of hot magmatic rocks [*Allen and Seyfried*, 2004; *Douville et al.*, 2002]. These vents are therefore probably active during periods when gabbroic or doleritic bodies are emplaced and cooled within, or immediately below the permeable upper lithosphere next to the axial exhumation fault (Figures 3c and 11b) [*McCaig et al.*, 2007].

Permeabilities in this domain must be sufficient to maintain a vigorous hydrothermal convection and counteract the water consumption associated with serpentinization reactions [*Emmanuel and Berkowitz*, 2006]. In addition, serpentinization results in a substantial volume increase (about 30% for 100% serpentinization) [*Komor et al.*, 1985; *O'Hanley*, 1992]. This will tend to close fluid pathways, which must therefore be frequently reactivated in order for serpentinization to proceed. We know little of the characteristics (permeabilities, lateral and depth extent, and time variability of these parameters) of the permeable footwall domain. The interpretation of seismic velocities in terms of degree of serpentinization is nonunique (Figure 5) and probably represents the end-product of a complex history of deformation and serpentinization. Sampling, which offers the opportunity to unravel this history [*Andreani et al.*, 2007], is restricted to within a few hundred meters of the main detachment fault.

Seismic data do, however, indicate that ultramafic rocks emplaced more than 3–4 km below seafloor are generally not serpentinized. This indicates that the permeable domain of active serpentinization probably does not extend more than 3–4 km into the footwall of the axial exhumation fault (Figure 10). In Figure 10, we hypothesize that this corresponds to the maximum thickness of the permeable domain, at any given time during the exhumation of the ultramafics. We note that this 3- to 4-km-thick inferred permeable domain has the same dimensions as the domain of persistent seismicity next to the detachment in the Trans-Atlantic Geotraverse (TAG) region of the MAR [*deMartin et al.*, 2007]. The TAG hydrothermal field is basalt-hosted but resembles R and L in terms of tectonic setting next to a large detachment fault [*Tivey et al.*, 2003]. This leads us to propose that frequent brittle failure caused by tectonic stress accumulation in the footwall of the detachment may generate and maintain the fluid paths needed for serpentinization to proceed.

We also do not know very much about the location and the depth of emplacement of the magmatic bodies, which are involved in fluid-rock reactions feeding R- or L-type hydrothermal vents. Current interpretative models are two-dimensional and emphasize across-axis hydrothermal circulations [*deMartin et al.*, 2007; *McCaig et al.*, 2007], with inferred magmatic bodies located at depth along the same flow line as the venting areas. Ridge-parallel fractures and fissures caused by spreading-related tensional stresses [*Barclay and Toomey*, 2003] may, however, be predicted to favor along-axis hydrothermal circulations [*Nehlig and Juteau*, 1988], which may therefore interact with magmatic bodies located some distance along-axis. This may be the case in the TAG area, where there is no seismic evidence for a shallow magma body immediately below the vent field [*Canales et al.*, 2007].

By contrast, the LC field is set on off-axis basement, next to a transform fault [*Fruh-Green et al.*, 2003], and no comparable vents have yet been described within the confines of a slow spreading ridge axial valley. Such axial white smokers could, however, have gone undetected because their plumes are weak and nearly devoid of particulate matter. This possibility is discussed by *Baker et al.* [2004] based on plume studies at the low melt supply SWIR and Gakkel ridges. In addition, serpentinization-derived fluids of yet lower temperatures may also vent in a more diffuse fashion. This may be the cause of the methane anomalies measured in seawater a few meters above ultramafic outcrops in the MAR 15°N region [*Charlou et al.*, 1998]. Q5

LC-type white smokers, and more diffuse low temperature vents, may therefore be the dominant vectors of serpentinization-derived fluids in ultramafic-dominated axial contexts, when little or no melt is being emplaced within the reach of hydrothermal circulations (Figure 10a). In melt-poor and ultraslow ridge regions, such as the easternmost SWIR or central Gakkel Ridge [*Cannat et al.*, 2006; *Michael et al.*, 2003], this could be the dominant serpentinization setting. At the MAR, however, this could be a limited setting because volcanism is ubiquitous, and therefore, the time intervals between successive melt intrusions may be relatively short, particularly if hydrothermal circulation has an along-axis component and can therefore access magmatic bodies located some distance along-axis from the venting areas.

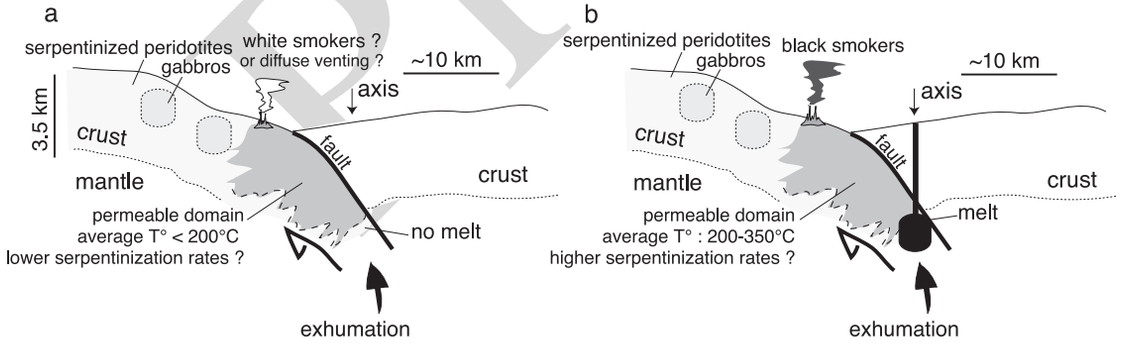

Figure 10. A conceptual model of serpentinization at slow and ultraslow spreading ridges, based on discussion in text. We identify two distinct settings: (a) one may be characteristic of magma-poor ridge domains and (b) the other of less magma-poor domains, where gabbro intrusions are frequently emplaced within exhumed ultramafics, or along-axis within reach of the hydrothermal circulations involved in serpentinizing the ultramafics. We infer that the permeable domain where these circulations take place is primarily controlled by detachment-related tectonics. It extends to a maximum of 3 to 4 km into the detachment footwall. In periods when there is no melt emplaced near this permeable domain (Figure 10a), we propose that its overall temperature may become too low for rapid serpentinization to occur [*Martin and Fyfe*, 1970]. By contrast, in periods when melt comes near this permeable domain, high temperature hydrothermal circulations may promote rapid serpentinization (Figure 10b).

The question therefore arises of which type of hydrothermal circulation contributes most to the serpentinization of the ultramafic component of the crust, and whether there are significant differences in serpentinization-related fluxes between normal melt supply and low melt supply ridge regions (Figure 10). Our flux estimates can be used as guidelines for this discussion and to plan for the acquisition of new data. For example, if serpentinization-derived fluids are mostly expelled in R-type hydrothermal systems (hypothesis 1), then the relatively low time-averaged initial hydrogen flux estimated with the second method (QH_2heat Initial in Table 2, and red star in Figure 9) is more consistent (Figure 9) with a finite serpentinization pattern involving a maximum serpentinization ≤86% and relatively low hydrogen production rates (curve b in Figure 7). Alternatively, serpentinization occurring mostly in LC-type hydrothermal systems (hypothesis 2) would require a finite serpentinization pattern with a higher maximum degree of serpentinization and higher hydrogen production rates (upper star in Figure 9). Detailed studies of serpentinized suites from more slow spreading ridge locations would allow to test this empirical prediction, and coupled experimental studies would help identify which parameters of the hydrothermal system control magnetite and hydrogen production rates during serpentinization.

Additional constraints may be derived from the specific case of R because it is, so far, the only ultramafic-hosted ridge vent field for which we have estimates of the total fluid, heat, and hydrogen fluxes [*Jean-Baptiste et al.*, 2004]. In hypothesis 1 (R-type systems dominant), these fluxes correspond to more than 100 km worth of our time-integrated estimates (see the end of section 4.3). Although this ridge length may be overestimated (because average hydrothermal heat loss may be higher and because part of the hydrogen produced may have been consumed by subseafloor organisms), we have argued that it seems too large because the along-axis length of domains with frequent ultramafic outcrops surrounding the R field (Plate 1) is probably <50 km. One explanation would be that exhumation rates at R are currently higher than the half spreading rate, as suggested, for example, by zircon dating for the Atlantis Massif detachment fault (MAR 30°N) [*Grimes et al.*, 2008]. Another explanation could be that serpentinization is not a steady state process but occurs in pulses during which more fresh peridotite is altered than provided by steady state extension and exhumation, alternating with periods of lower serpentinization rates. Further investigations of the factors, which may control serpentinization rates and their variability, are therefore needed.

In Figure 10, we suggest, as a working hypothesis, that serpentinization rates may be modulated by variations of the average temperature in the permeable domain beneath the exhumation fault, between periods of melt emplacement. Serpentinization rates are highest at temperatures between 200° and 350°C [*Martin and Fyfe*, 1970], and most serpentinized peridotite samples from the MAR have oxygen isotopic signatures consistent with such high temperatures of serpentinization [e.g., *Fruh-Green et al.*, 2004]. We infer that in periods when axial hydrothermal cells cannot access a magmatic heat source because it is either absent or too deep to connect to the permeable zone, the average temperature in this permeable zone may become too low for serpentinization to occur at high rates (Figure 10a). Higher temperature hydrothermal fluids produced during a subsequent period of melt intrusion would therefore have access to a higher volume of incompletely serpentinized peridotite (Figure 10b). This model would also suggest that exhumed ultramafics at magma-poor ridges (easternmost SWIR or central Gakkel Ridge) may be serpentinized at lower overall temperatures and possibly to a lesser extent (although lower spreading rate may compensate for the lower rates of serpentinization because the exhumed ultramafics are allowed more time in the permeable footwall of axial detachment faults).

6. CONCLUSIONS

The principal conclusions of this chapter can be summarized as follows:

1. Domains with frequent outcrops of exhumed mantle-derived ultramafics are estimated to represent about 23% of the seafloor created at ridges spreading at rates less than 40 mm a^{-1}. Mantle exhumation would occur along asymmetric detachment faults along about 14,660 km of the present-day ridge system, with an average exhumation rate of 11.4 mm a^{-1}. Domains of ultramafic seafloor also expose gabbro intrusions and basalts in proportions estimated between 30% and 50% at the MAR and less than 10% in melt-poor regions of ultraslow spreading ridges.

2. Serpentinization occurs while mantle-derived ultramafics are being exhumed in the footwall of large offset axial normal faults. It extends to a maximum of 3 to 4 km within the fault's footwall. It results in hydrogen and methane fluxes, which depend primarily on iron speciation in serpentinization reaction products. We use two independent methods to estimate these fluxes. Both methods yield values that correspond to averages over the time it takes for the newly exhumed material to leave the axial domain. Serpentinization-related initial (prior to methane production) hydrogen fluxes obtained with the two approaches have a wide range of possible values, yet they do overlap, and we argue that the most likely flux values in ridge domains, where mantle exhumation occurs, correspond to about 10^7 mol a^{-1} and per

kilometer of ridge axis, for an exhumation rate of 10 mm a^{-1}. This preferred flux estimate would yield a global hydrogen flux of about 16.7×10^{10} mol a^{-1} for present-day mid-ocean ridges, of which about 15% would react to form methane. This would correspond to an estimated global methane flux due to serpentinization at mid-ocean ridges of about 2.5×10^{10} mol a^{-1}, or 0.4 Mt a^{-1}, a small number compared with the estimated global methane flux to the atmosphere of 500 Mt a^{-1} [*Cicerone and Oremland*, 1988].

3. The two independent methods we use to estimate serpentinization-related hydrogen fluxes involve distinct causes of uncertainties, having to do with the distribution and mineralogy of serpentinization reactions, and with the nature of associated hydrothermal circulations. In the discussion, we develop a conceptual model, which relates fluid circulation and serpentinization to the distribution of brittle fracture and faulting in the detachment fault's footwall. We distinguish between two settings. In one setting, melt is being emplaced and cooled in the exhumed ultramafics next to this fractured permeable domain, resulting in R-type black smoker fluids. In the other setting, no melt is being emplaced next to the permeable serpentinization domain. We propose that serpentinization in this latter case may occur at lower average temperatures and at slower rates.

Acknowledgments. We thank our two anonymous reviewers for their most helpful comments. We are also grateful to the editors of this volume for their efforts. Our work was partly funded by the "Action Incitative Hydrogène" of CNRS-INSU. It benefited from discussions with Adélie Delacour, Andy McCaig, Gretchen Früh-Green, Catherine Mével, and Muriel Andréani. This is IPGP publication number 2434.

REFERENCES

Allen, D. E., and W. E. Seyfried (2004), Serpentinization and heat generation: Constraints from Lost City and rainbow hydrothermal systems, *Geochim. Cosmochim. Acta*, *68*, 1347–1354.

Andreani, M., C. Mével, A.-M. Boullier, and J. Escartín (2007), Dynamic control on serpentine crystallization in veins: Constraints on hydration processes in oceanic peridotites, *Geochem. Geophys. Geosyst.*, *8*, Q02012, doi:10.1029/2006GC001373.

Aumento, F., and H. Loubat (1971), The Mid-Atlantic Ridge near 45°N. Serpentinized ultramafic intrusions, *Can. J. Earth Sci.*, *8*, 631–663.

Bach, W., C. J. Garrido, H. Paulick, J. Harvey, and M. Rosner (2004), Seawater-peridotite interactions: First insights from ODP Leg 209, MAR 15°N, *Geochem. Geophys. Geosyst.*, *5*, Q09F26, doi:10.1029/2004GC000744.

Bach, W., H. Paulick, C. J. Garrido, B. Ildefonse, W. P. Meurer, and S. E. Humphris (2006), Unraveling the sequence of serpentinization reactions: Petrography, mineral chemistry, and petrophysics of serpentinites from MAR 15°N (ODP Leg 209, Site 1274), *Geophys. Res. Lett.*, *33*, L13306, doi:10.1029/2006GL025681.

Baker, E. T. (2007), Hydrothermal cooling of midocean ridge axes: Do measured and modeled heat fluxes agree?, *Earth Planet. Sci. Lett.*, *263*, 140–150.

Baker, E. T., H. N. Edmonds, P. J. Michael, W. Bach, H. J. B. Dick, J. E. Snow, S. L. Walker, N. R. Banerjee, and C. H. Langmuir (2004), Hydrothermal venting in magma deserts: The ultraslow-spreading Gakkel and Southwest Indian Ridges, *Geochem. Geophys. Geosyst.*, *5*, Q08002, doi:10.1029/2004GC000712.

Barclay, A. H., and D. R. Toomey (2003), Shear wave splitting and crustal anisotropy at the Mid-Atlantic Ridge, 35°N, *J. Geophys. Res.*, *108*(B8), 2378, doi:10.1029/2001JB000918.

Barclay, A. H., D. R. Toomey, and S. C. Solomon (2001), Microearthquake characteristics and crustal Vp/Vs structure at the Mid-Atlantic Ridge, 35°N, *J. Geophys. Res.*, *106*, 2017–2034.

Beltenev, V., V. Ivanov, A. Shagin, S. M., R. I., V. Shilov, I. Dovretzova, G. Cherkashev, M. Samovarov, and I. Poroshina (2005), New hydrothermal sites at 13°N, Mid Atlantic Ridge, *InterRidge News*, *14*, 14–16. Q6

Berndt, M. E., D. E. Allen, and W. E. Seyfried (1996), Reduction of CO_2 during serpentinization of olivine at 300°C and 500 bar, *Geology*, *24*, 351–354.

Beslier, M. O., J. Girardeau, and G. Boillot (1990), Kinematics of peridotite emplacement during North Atlantic continental rifting, Galicia, northwestern Spain, *Tectonophysics*, *184*, 321–343.

Bird, P. (2003), An updated digital model of plate boundaries, *Geochem. Geophys. Geosyst.*, *4*(3), 1027, doi:10.1029/2001GC000252.

Boillot, G., G. Féraud, M. Recq, and J. Girardeau (1989), Undercrusting by serpentine beneath rifted margins, *Nature*, *341*, 523–525.

Bougault, H., J.-L. Charlou, Y. Fouquet, H. D. Needham, N. Vaslet, P. Appriou, P. Jean Baptiste, P. A. Rona, L. Dimitriev, and S. Silantiev (1993), Fast and slow spreading ridges: Structure and hydrothermal activity, ultramafic topographic highs and CH_4 output, *J. Geophys. Res.*, *98*, 9643–9651.

Brudzinski, M. R., C. H. Thurber, B. R. Hacker, and E. R. Engdahl (2007), Global prevalence of double Benioff Zones, *Science*, *316*, 1472–1474.

Buck, R. W. (1988), Flexural rotation of normal faults, *Tectonics*, *7*, 959–973.

Buck, W. R., L. Lavier, and A. Poliakov (2005), Modes of faulting at mid-ocean ridges, *Nature*, *434*, 719–723.

Canales, J. P., J. A. Collins, J. Escartin, and R. S. Detrick (2000), Seismic structure across the rift valley of the Mid-Atlantic ridge at 23°20′N (MARK area): Implications for crustal accretion processes at slow-spreading ridges, *J. Geophys. Res.*, *105*, 28,411–28,425.

Canales, J. P., R. A. Sohn, and B. J. Demartin (2007), Crustal structure of the Trans-Atlantic Geotraverse (TAG) segment (Mid-Atlantic Ridge, 26°10′N): Implications for the nature of hydrothermal circulation and detachment faulting at slow spreading ridges, *Geochem. Geophys. Geosyst.*, *8*, Q08004, doi:10.1029/2007GC001629.

Cann, J. R., D. K. Blackman, D. K. Smith, E. McAllister, B. Janssen, S. Mello, E. Avgerinos, A. R. Pascoe, and J. Escartín

(1997), Corrugated slip surfaces formed at North Atlantic ridge-transform intersections, *Nature*, *385*, 329–332.

Cannat, M. (1993), Emplacement of mantle rocks in the seafloor at mid-ocean ridges, *J. Geophys. Res.*, *98*, 4163–4172.

Cannat, M. (1996), How thick is the magmatic crust at slow spreading oceanic ridges?, *J. Geophys. Res.*, *101*, 2847–2857.

Cannat, M., and J. F. Casey (1995), An ultramafic lift at the Mid-Atlantic Ridge: Successive stages of magmatism in serpentinized peridotites from the 15°N region, in *Mantle and Lower Crust Exposed in Oceanic Ridges and in Ophiolites*, edited by R. L. M. Vissers and A. Nicolas, pp. 5–34, Springer, The Netherlands.

Cannat, M., et al. (1995), Thin crust, ultramafic exposures, and rugged faulting patterns at the Mid-Atlantic Ridge (22°–24°N), *Geology*, *23*, 49–52.

Cannat, M., F. Chatin, H. Whitechurch, and G. Ceuleneer (1997a), Gabbroic rocks trapped in the upper mantle at the mid-Atlantic ridge, in *Proc. Ocean Drill. Program Sci. Results*, vol. 153, edited by J. A. Karson et al., pp. 243–264, Ocean Drill. Program, College Station, TX.

Cannat, M., Y. Lagabrielle, H. Bougault, J. Casey, N. de Coutures, L. Dmitriev, and Y. Fouquet (1997b), Ultramafic and gabbroic exposures at the Mid-Atlantic Ridge: Geological mapping in the 15°N region, *Tectonophysics*, *279*, 193–213.

Cannat, M., et al. (1999a), Mid-Atlantic ridge—Azores hotspot interactions: Along-axis migration of a hotspot-derived magmatic pulse 14 to 4 myrs ago, *Earth Planet. Sci. Lett.*, *173*, 257–269.

Cannat, M., C. Rommevaux-Jestin, D. Sauter, C. Deplus, and V. Mendel (1999b), Formation of the axial relief at the very slow spreading Southwest Indian Ridge (49°–69°E), *J. Geophys. Res.*, *104*, 22,825–22,843.

Cannat, M., C. Rommevaux-Jestin, and H. Fujimoto (2003), Melt supply variations to a magma-poor ultra-slow spreading ridge (Southwest Indian Ridge 61° to 69°E), *Geochem. Geophys. Geosyst.*, *4*(8), 9104, doi:10.1029/2002GC000480.

Cannat, M., J. R. Cann, and J. Maclennan (2004), Some hard rock constraints on the heat supply to mid-ocean ridges, in *Mid-Ocean Ridges: Hydrothermal Interactions between the Lithosphere and Oceans*, *Geophys. Monogr. Ser.*, vol. 148, edited by C. German, J. Lin, and L. Parson, pp. 111–150, AGU, Washington, D. C.

Cannat, M., D. Sauter, V. Mendel, E. Ruellan, K. Okino, J. Escartin, V. Combier, and M. Baala (2006), Modes of seafloor generation at a melt-poor ultra-slow-spreading ridge, *Geology*, *34*, 605–608.

Cannat, M., D. Sauter, A. Bezos, C. Meyzen, E. Humler, and M. Le Rigoleur (2008), Spreading rate, spreading obliquity, and melt supply at the ultraslow spreading Southwest Indian Ridge, *Geochem. Geophys. Geosyst.*, *9*, Q04002, doi:10.1029/2007GC001676.

Carlson, R. L. (2001), The abundance of ultramafic rocks in Atlantic oceanic crust, *Geophys. J. Int.*, *144*, 37–48.

Carlson, R. L., and D. J. Miller (1997), A new assessment of the abundance of serpentinite in the oceanic crust, *Geophys. Res. Lett.*, *24*, 457–460.

Casey, J. F. (1981), Heterogeneous nature of the oceanic crust and upper mantle: A perspective from the Bay of Island ophiolite complex, in *The Sea*, vol. 7, edited by C. Emiliani, pp. 305–338, John Wiley, New York.

Charlou, J.-L., and J.-P. Donval (1993), Hydrothermal methane venting between 12°N and 26°N along the Mid-Atlantic ridge, *J. Geophys. Res.*, *98*, 9625–9642.

Charlou, J. L., Y. Fouquet, H. Bougault, J. P. Donval, J. Etoubleau, P. Jean-Baptiste, A. Dapoigny, P. Appriou, and P. A. Rona (1998), Intense CH_4 plumes generated by serpentinization of ultramafic rocks at the intersection of the 15°20′N fracture zone and the Mid-Atlantic Ridge, *Geochim. Cosmochim. Acta*, *62*, 2323–2333.

Charlou, J. L., J. P. Donval, Y. Fouquet, P. Jean-Baptiste, and N. Holm (2002), Geochemistry of high H_2 and CH_4 vent fluids issuing from ultramafic rocks at the Rainbow hydrothermal field (36°14′N, MAR), *Chem. Geol.*, *191*, 345–359.

Chen, Y., and W. J. Morgan (1990), A nonlinear rheology model for mid-ocean ridge axis topography, *J. Geophys. Res.*, *95*, 17,583–17,604.

Chen, Y. J. (1992), Oceanic crustal thickness versus spreading rate, *Geophys. Res. Lett.*, *19*, 753–756.

Chen, Y. J., and J. Phipps Morgan (1996), The effects of spreading rate, the magma budget, and the geometry of magma emplacement on the axial heat flux at mid-ocean ridges, *J. Geophys. Res.*, *101*, 11,475–11,482.

Christensen, N. I. (1966), Elasticity of ultrabasic rocks, *J. Geophys. Res.*, *71*, 5921–5931.

Christensen, N. I. (1972), The abundance of serpentinites in the oceanic crust, *J. Geol.*, *80*, 709–719.

Cicerone, R. J., and R. S. Oremland (1988), Biogeochemical aspects of atmospheric methane, *Global Biogeochem. Cycles*, *2*, 299–327.

Collier, J., and M. Sinha (1990), Seismic images of a magma chamber beneath the Lau Basin back-arc spreading center, *Nature*, *346*, 646–648.

Davydov, M. P., P. A. Aleksandrov, E. N. Perova, and T. A. Semkova (2007), Ferromanganese deposits in the Ashadze-1 hydrothermal field (Mid-Atlantic Ridge, 12°58′N), *Dokl. Earth Sci.*, *415*, 954–960.

deMartin, B. J., R. A. Sohn, J. P. Canales, and S. Humphris (2007), Kinematics and geometry of active detachment faulting beneath the Trans-Atlantic Geotraverse (TAG) hydrothermal field on the Mid-Atlantic Ridge, *Geology*, *35*, 711–714.

DeMets, C., R. G. Gordon, D. F. Argus, and S. Stein (1994), Effect of recent revisions to the geomagnetic reversal time scale on estimates of current plate motions, *Geophys. Res. Lett.*, *21*, 2191–2194.

Deplus, C., M. Maïa, D. Aslanian, and P. Gente (1992), Segmentation of the Mid-Atlantic Ridge south of Kane fracture zone revealed by gravity anomalies: Results of SEADMA 1 cruise, *Eos Trans. AGU*, *73*, 568.

Detrick, R. S., P. Buhl, E. Vera, J. Mutter, J. Orcutt, J. Madsen, and T. Brocher (1987), Multichannel seismic imaging of a crustal magma chamber along the East Pacific Rise between 9°N and 13°N, *Nature*, *326*, 35–41.

Detrick, R., J. Collins, and S. Swift (1994), In situ evidence for the nature of the seismic layer 2/3 boundary in oceanic crust, *Nature*, *370*, 288–290.

Dias, A. S., and F. Barriga (2006), Mineralogy and geochemistry of hydrothermal sediments from the serpentinite-hosted Saldanha

hydrothermal field (36°34′N; 33°26′W) at MAR, *Mar. Geol.*, *225*, 157–175.

Dick, H. J. B. (1989), Abyssal peridotites, very slow spreading ridges and ocean ridge magmatism, in *Magmatism in the Ocean Basins*, *Geol. Soc. Spec. Publ.*, vol. 24, edited by A. D. Saunders and M. J. Norry, pp. 71–105.

Dick, H. J. B., J. Lin, and H. Schouten (2003), An ultraslow-spreading class of ocean ridge, *Nature*, *426*, 405–412.

Dick, H. J. B., M. A. Tivey, and B. E. Tucholke (2008), Plutonic foundation of a slow-spreading ridge segment: The oceanic core complex at Kane Megamullion, 23°30′N, 45°20′W, *Geochem. Geophys. Geosyst.*, *9*, Q05014, doi:10.1029/2007GC001645.

Dilek, Y., A. Coulton, and S. D. Hurst (1997), Serpentinization and hydrothermal veining in peridotites at site 920D in the MARK area, in *Proc. Ocean Drill. Program Sci. Results*, vol. 153, edited by J. A. Karson et al., pp. 35–59, Ocean Drill. Program, College Station, TX.

Douville, E., J. L. Charlou, E. H. Oelkers, P. Bienvenu, C. F. J. Colon, J. P. Donval, Y. Fouquet, D. Prieur, and P. Appriou (2002), The Rainbow vent fluids (36°14′N, MAR): The influence of ultramafic rocks and phase separation on trace metal content in Mid-Atlantic Ridge hydrothermal fluids, *Chem. Geol.*, *184*, 37–48.

Emmanuel, S., and J. J. Ague (2007), Implications of present-day abiogenic methane fluxes for the early Archean atmosphere, *Geophys. Res. Lett.*, *34*, L15810, doi:10.1029/2007GL030532.

Emmanuel, S., and B. Berkowitz (2006), Suppression and stimulation of seafloor hydrothermal convection by exothermic mineral hydration, *Earth Planet. Sci. Lett.*, *243*, 657–668.

Escartín, J., and M. Cannat (1999), Ultramafic exposures and the gravity signature of the lithosphere near the Fifteen-Twenty Fracture Zone (Mid-Atlantic Ridge, 14°–16.5°N), *Earth Planet. Sci. Lett.*, *171*, 411–424.

Escartín, J., G. Hirth, and B. Evans (1997), Effects of serpentinization on the lithospheric strength and the style of normal faulting at slow-spreading ridges, *Earth Planet. Sci. Lett.*, *151*, 181–190.

Escartín, J., G. Hirth, and B. Evans (2001), Strength of slightly serpentinized peridotites: Implications of the tectonics of oceanic lithosphere, *Geology*, *29*, 1023–1026.

Escartin, J., C. Mével, C. J. MacLeod, and A. M. McCaig (2003), Constraints on deformation conditions and the origin of oceanic detachments: The Mid-Atlantic Ridge core complex at 15°45′N, *Geochem. Geophys. Geosyst.*, *4*(8), 1067, doi:10.1029/2002GC000472.

Escartin, J., M. Andreani, G. Hirth, and B. Evans (2008), Relationships between the microstructural evolution and the rheology of talc at elevated pressures and temperatures, *Earth Planet. Sci. Lett.*, *268*, 463–475.

Foustoukos, D. I., and W. E. Seyfried (2004), Hydrocarbons in hydrothermal vent fluids: The role of chromium-bearing catalysts, *Science*, *304*, 1002–1005.

Frost, B. R. (1985), On the stability of sulfides, oxides, and native metals in serpentinite, *J. Petrol.*, *26*, 31–63.

Fruh-Green, G. L., D. S. Kelley, S. M. Bernasconi, J. A. Karson, K. A. Ludwig, D. A. Butterfield, C. Boschi, and G. Proskurowski (2003), 30,000 years of hydrothermal activity at the Lost City vent field, *Science*, *301*, 495–498.

Fruh-Green, G. L., J. A. D. Connolly, and A. Plas (2004), Serpentinization of oceanic peridotites: Implications for geochemical cycles and biological activity, in *The Subseafloor Biosphere at Mid-Ocean Ridges*, *Geophys. Monogr. Ser.*, vol. 144, edited by W. S. D. Wilcock et al., pp. 119–136, AGU, Washington, D. C.

Fujiwara, T., J. Lin, P. B. Matsumoto, B. Tucholke, and J. F. Casey (2003), Crustal evolution of the Mid-Atlantic Ridge near the Fifteen-Twenty Fracture Zone in the last 5 Ma, *Geochem. Geophys. Geosyst.*, *4*(3), 1024, doi:10.1029/2002GC000364.

Fyfe, W. S. (1974), Heats of chemical reactions and submarine heat production, *Geophys. J. R. Astron. Soc.*, *37*, 213–215.

German, C. R., K. J. Richards, M. D. Rudnicki, M. M. Lam, and J. L. Charlou (1998), Topographic control of a dispersing hydrothermal plume, *Earth Planet. Sci. Lett.*, *156*, 267–273.

Gràcia, E., J. L. Charlou, J. R. Radford-Knoery, and L. M. Parson (2000), Non-transform offsets along the Mid-Atlantic Ridge south of the Azores (38°N–34°N): Ultramafic exposures and hosting of hydrothermal vents, *Earth Planet. Sci. Lett.*, *177*, 89–103.

Grimes, C., B. Craig, B. E. John, M. J. Cheadle, and J. L. Wooden (2008), Protracted construction of gabbroic crust at a slow spreading ridge: Constraints from 206Pb/238U zircon ages from Atlantis Massif and IODP Hole U1309D (30°N, MAR), *Geochem. Geophys. Geosyst.*, *9*, Q08012, doi:10.1029/2008GC002063.

Hess, H. H. (1962), History of ocean basins, in *Petrologic Studies, the Burlington Volume*, edited by A. E. J. Engel, H. L. James, and B. F. Leonard, pp. 599–620, Geological Society of America, Boulder, CO.

Hirth, G., J. Escartín, and J. Lin (1998), The rheology of the lower oceanic crust: Implications for lithospheric deformation at Mid-Ocean ridges, in *Faulting and Magmatism at Mid-ocean Ridges*, *Geophys. Monogr. Ser.*, vol. 106, edited by W. R. Buck et al., pp. 291–303, AGU, Washington, D. C.

Horen, H., M. Zamora, and G. Dubuisson (1996), Seismic waves velocities and anisotropy in serpentinized peridotites from Xigaze ophiolite: Abundance of serpentine in slow spreading ridges, *Geophys. Res. Lett.*, *23*, 9–12.

Horita, J., and M. E. Berndt (1999), Abiogenic methane formation and isotopic fractionation under hydrothermal conditions, *Science*, *285*, 1055–1057.

Humphris, S. E., and J. R. Cann (2000), Constraints on the energy and chemical balances of the modern TAG and ancient Cyprus seafloor sulfide deposits, *J. Geophys. Res.*, *105*, 28,477–28,488.

Jean-Baptiste, P., E. Fourre, J. L. Charlou, C. R. German, and J. Radford-Knoery (2004), Helium isotopes at the Rainbow hydrothermal site (Mid-Atlantic Ridge, 36°14′N), *Earth Planet. Sci. Lett.*, *221*, 325–335.

Jokat, W., O. Ritzmann, M. C. Schmidt-Aursch, S. Drachev, S. Gauger, and J. Snow (2003), Geophysical evidence for reduced melt production on the Arctic ultraslow Gakkel mid-ocean ridge, *Nature*, *423*, 962–965.

Kadko, D., N. D. Rosenberg, J. E. Lupton, R. W. Collier, and M. D. Lilley (1990), Chemical reaction rates and entrainment within the Endeavour Ridge hydrothermal plume, *Earth Planet. Sci. Lett.*, *120*, 361–374.

Karson, J. A. (1990), Seafloor spreading on the Mid-Atlantic Ridge: Implications for the structure of ophiolites and oceanic

lithosphere produced in slow-spreading environments, in *Proceedings of the Symposium "Troodos 1987"*, edited by J. Malpas et al., pp. 547–555, Cyprus Geological Survey Department, Nicosia.

Karson, J. A., (1991), Seafloor spreading on the Mid-Atlantic Ridge: Implications for the structure of ophiolites and oceanic lithosphere produced in slow-spreading environments, in *Proceedings of Symposium "Troodos 1987"*, edited by J. Malpas et al., Geological Survey Department, Cyprus.

Karson, J. A., and H. J. B. Dick (1984), Deformed and metamorphosed crust at the mid-Atlantic ridge, *Ofioliti*, *9*, 279–302.

Karson, J. A., et al. (1987), Along-axis variations in seafloor spreading in the MARK Area, *Nature*, *328*, 681–685.

Kasting, J. F., and D. Catling (2003), Evolution of a habitable planet, *Annu. Rev. Astron. Astrophys.*, *41*, 429–463.

Kelley, D. S., et al. (2001), An off-axis hydrothermal vent field near the Mid-Atlantic Ridge at 30°N, *Nature*, *411*, 145–149.

Kelley, D. S., et al. (2005), A serpentinite-hosted ecosystem: The Lost City hydrothermal field, *Science*, *307*, 1428–1434.

Kent, G. M., A. J. Harding, and J. Orcutt (1993), Distribution of magma beneath the East Pacific Rise between the Clipperton transform and the 9°17′N Deval from forward modeling of common depth point data, *J. Geophys. Res.*, *98*, 13,945–13,969.

Komor, S. C., D. Elthon, and J. F. Casey (1985), Serpentinization of cumulate ultramafic rocks from the North Arm Mountain massif of the Bay of Islands ophiolite, *Geochim. Cosmochim. Acta*, *49*, 2331–2338.

Kuo, B. Y., and D. W. Forsyth (1988), Gravity anomalies of the ridge-transform system in the South Atlantic between 31° and 34.5°S: Upwelling centers and variation in crustal thickness, *Mar. Geophys. Res.*, *10*, 205–232.

Lavier, L., W. R. Buck, and A. N. B. Poliakov (1999), Self-consistent rolling-hinge model for the evolution of large-offset low-angle normal faults, *Geology*, *27*, 1127–1130.

Lin, J., G. M. Purdy, H. Schouten, J. C. Sempere, and C. Zervas (1990), Evidence from gravity data for focused magmatic accretion along the Mid-Atlantic Ridge, *Nature*, *344*, 627–632.

Lowell, R. P. (2007), Numerical simulations of single-pass hydrothermal convection at mid-ocean ridges: Effects of the extrusive layer and temperature-dependent permeability, *Geochem. Geophys. Geosyst.*, *8*, Q10011, doi:10.1029/2007GC001653.

Magde, L. S., D. W. Sparks, and R. S. Detrick (1997), The relationship between buoyant mantle flow, melt migration and bull's eyes at the Mid-Atlantic Ridge between 33°N and 35°N, *Earth Planet. Sci. Lett.*, *148*, 59–67.

Maia, M., and P. Gente (1998), Three-dimensional gravity and bathymetry analysis of the Mid-Atlantic Ridge between 20°N and 24°N: Flow geometry and temporal evolution of the segmentation, *J. Geophys. Res.*, *103*, 951–974.

Martin, B., and W. S. Fyfe (1970), Some experimental and theoretical observations on the kinetics of hydration reactions with particular reference to serpentinization, *Chem. Geol.*, *6*, 185–202.

McCaig, A. M., R. A. Cliff, J. Escartin, A. E. Fallick, and C. J. MacLeod (2007), Oceanic detachment faults focus very large volumes of black smoker fluids, *Geology*, *35*, 935–938.

Michael, P. J., et al. (2003), Magmatic and amagmatic seafloor generation at the ultraslow-spreading Gakkel ridge, Arctic Ocean, *Nature*, *423*, 956–961.

Miller, D. J., and N. I. Christensen (1997), Seismic velocities of lower crustal and upper mantle rocks from the slow-spreading mid-Atlantic ridge, south of the Kane Transform zone (MARK), *Proc. Ocean Drill. Program Sci. Results*, *153*, 437–454.

Minshull, T. A., M. R. Muller, C. J. Robinson, R. S. White, and M. J. Bickle (1998), Is the oceanic Moho a serpentinization front?, in *Modern Ocean Floor Processes and the Geological Record*, *Geol. Soc., London, Spec. Publ.*, vol. 148, edited by R. A. Mills and K. Harrison, pp. 71–80, Geol. Soc. London, London.

Minshull, T. A., M. R. Muller, and R. S. White (2006), Crustal structure of the Southwest Indian Ridge at 66°E: Seismic constraints, *Geophys. J. Int.*, *166*, 135–147.

Moody, J. B. (1976), Serpentinization: A review, *Lithos*, *9*, 126–138.

Moore, D. E., and D. A. Lockner (2008), Talc friction in the temperature range 25°–400°C: Relevance for fault-zone weakening, *Tectonophysics*, *449*, 120–132.

Mottl, M. J. (2003), Partitioning of energy and mass fluxes between mid-ocean ridge axes and flanks at high and low temperature, in Energy and Mass Transfer in Marine Hydrothermal Systems, edited by P. E. Halbach, V. Tunnicliffe, and J. R. Hein, pp. 271–286, Dahlem Univ. Press.

Mottl, M. J., and C. G. Wheat (1994), Hydrothermal circulation through midocean ridge flanks. Fluxes of heat and magnesium, *Geochem. Cosmochim. Acta*, *58*, 2225–2237.

Muller, M. R., T. A. Minshull, and R. S. White (1999), Segmentation and melt supply at the Southwest Indian Ridge, *Geology*, *27*, 867–870.

Murton, B., S. Unsworth, M. Harris, C. MacLeod, R. Searle, J. Casey, K. Achenbach, and C. Mallows (2007), Fluid flow at active oceanic core complexes, 13°N Mid-Atlantic Ridge, *Eos Trans. AGU*, *88*, Fall Meet. Suppl., Abstract T53B-1309.

Nehlig, P., and T. Juteau (1988), Flow porosities, permeabilities and preliminary data on fluid inclusions and fossil thermal gradients in the crustal sequence of the Sumail ophiolite (Oman), *Tectonophysics*, *151*, 199–221.

O'Hanley, D. S. (1992), Solution to the volume problem in serpentinization, *Geology*, *20*, 705–708.

Ophiolites (1972), Proceedings of the Penrose Conference on Ophiolites, pp. 24–25.

Oufi, O., M. Cannat, and H. Horen (2002), Magnetic properties of variably serpentinized abyssal peridotites, *J. Geophys. Res.*, *107*(B5), 2095, doi:10.1029/2001JB000549.

Pelayo, A. M., S. Stein, and C. A. Stein (1994), Estimation of oceanic hydrothermal heat flux from heat flow and depths of mid-ocean ridge seismicity and magma chambers, *Geophys. Res. Lett.*, *21*, 713–716.

Phipps Morgan, J., E. M. Parmentier, and J. Lin (1987), Mechanisms for the origin of Mid-Ocean Ridge axial topography: Implications for the thermal and mechanical structure of accreting plate boundaries, *J. Geophys. Res.*, *92*, 12,823–12,836.

Purdy, G. M., and R. S. Detrick (1986), Crustal structure of the Mid-Atlantic Ridge at 23°N from seismic refraction studies, *J. Geophys. Res.*, *91*, 3739–3762.

Raleigh, C. B., and M. B. Paterson (1965), Experimental deformation of serpentinite and its tectonic implications, *J. Geophys. Res.*, *70*, 3965–3985.

Reinen, L. A., J. D. Weeks, and T. E. Tullis (1991), The frictional behavior of serpentinite: Implications for aseismic creep on shallow crustal faults, *Geophys. Res. Lett.*, *18*, 1921–1924.

Rona, P. A., H. Bougault, J. L. Charlou, P. Appriou, T. A. Nelsen, J. H. Frey, G. L. Eberhart, and A. Barone (1992), Hydrothermal circulation, serpentinization, and degassing at a rift valley-fracture zone intersection: Mid-Atlantic Ridge near 15°N, 45°W, *Geology*, *20*, 783–786.

Severinghaus, J. P., and K. C. MacDonald (1988), High inside corners at ridge-transform intersections, *Mar. Geophys. Res.*, *9*, 353–367.

Seyfried, W. E., D. I. Foustoukos, and D. E. Allen (2004), Ultramafic-hosted hydrothermal systems at Mid-Ocean Ridges: Chemical and physical controls on pH, redox and carbon reduction reactions, in *Mid-Ocean Ridges: Hydrothermal Interactions Between the Lithosphere and Oceans*, *Geophys. Monogr. Ser.*, vol. 148, edited by C. German, J. Lin, and L. Parson, AGU, Washington, D. C.

Seyfried, W. E., D. I. Foustoukos, and Q. Fu (2007), Redox evolution and mass transfer during serpentinization: An experimental and theoretical study at 200°C, 500 bar with implications for ultramafic-hosted hydrothermal systems at Mid-Ocean Ridges, *Geochim. Cosmochim. Acta*, *71*, 3872–3886.

Seyler, M., M. Cannat, and C. Mevel (2003), Evidence for major-element heterogeneity in the mantle source of abyssal peridotites from the Southwest Indian Ridge (52° to 68°E), *Geochem. Geophys. Geosyst.*, *4*(2), 9101, doi:10.1029/2002GC000305.

Shipboard Scientific Party (1995), Site 920, in *Proc. Ocean Drill. Program Initial Rep.*, vol. 153, edited by M. Cannat, J. A. Karson, and D. J. Miller, pp. 45–119, Ocean Drill. Program, College Station, TX.

Shock, E. L., and M. E. Holland (2004), Geochemical energy sources that support the subsurface biosphere, in *The Subseafloor Biosphere at Mid-Ocean Ridges*, *Geophys. Monogr. Ser.*, vol. 144, edited by W. S. D. Wilcock et al., pp. 153–165, AGU, Washington, D. C.

Skelton, A., R. B. Whitmarsh, F. Arghe, P. Crill, and H. Koyi (2005), Constraining the rate and extent of mantle serpentinization from seismic and petrological data: Implications for chemosynthesis and tectonic processes, *Geofluids*, *5*, 153–164.

Sleep, N., and G. A. Barth (1997), The nature of the lower crust and shallow mantle emplacement at low spreading rates, *Tectonophysics*, *279*, 181–191.

Smith, D. K., J. Escartin, H. Schouten, and J. R. Cann (2008), Fault rotation and core complex formation: Significant processes in seafloor formation at slow-spreading mid-ocean ridges (Mid-Atlantic Ridge, 13°–15°N), *Geochem. Geophys. Geosyst.*, *9*, Q03003, doi:10.1029/2007GC001699.

Sorokhtin, O. G., A. Y. Lein, and I. E. Balanyuk (2001), Thermodynamics of oceanic hydrothermal systems and abiogenic methane generation, *Oceanology*, *41*, 861–872.

Spudich, P., and J. Orcutt (1980), A new look at the seismic velocity structure of the oceanic crust, *Rev. Geophys.*, *18*, 627–645.

Stein, C. A., and S. Stein (1994), Constraints on hydrothermal heat flux through the oceanic lithosphere from global heat flow, *J. Geophys. Res.*, *99*, 3081–3095.

Thibaud, R., P. Gente, and M. Maia (1998), A systematic analysis of the Mid-Atlantic Ridge morphology and gravity between 15°N and 40°N: Constraints of the thermal structure, *J. Geophys. Res.*, *103*, 24,233–24,243.

Tivey, M. A., H. Schouten, and M. C. Kleinrock (2003), A near-bottom survey of the Mid-Atlantic ridge axis at 26°N: Implications for the tectonic evolution of the TAG segment, *J. Geophys. Res.*, *108*(B5), 2277, doi:10.1029/2002JB001967.

Toft, P. B., J. Arkani-Hamed, and S. E. Haggerty (1990), The effect of serpentinization on density and magnetic susceptibility: A petrophysical model, *Phys. Earth Planet. Inter.*, *65*, 137–157.

Toomey, D. R., G. M. Purdy, and S. C. Solomon (1988), Microearthquakes beneath the median valley of the Mid-Atlantic ridge near 23°N: Tomography and tectonics, *J. Geophys. Res.*, *93*, 9093–9112.

Tucholke, B. E., and J. Lin (1994), A geological model for the structure of ridge segments in slow-spreading ocean crust, *J. Geophys. Res.*, *99*, 11,937–11,958.

Tucholke, B. E., K. Fujioka, T. Ishihara, G. Hirth, and M. Kinoshita (2001), Submersible study of an oceanic megamullion in the central North Atlantic, *J. Geophys. Res.*, *106*, 16,145–16,161.

Tucholke, B. E., M. D. Behn, R. Buck, and J. Lin (2008), Role of melt supply in oceanic detachment faulting and formation of megamullions, *Geology*, *36*, 455–458.

Ulmer, P., and V. Trommsdorff (1995), Serpentine stability to mantle depths and subduction-related magmatism, *Science*, *268*, 858–861.

Whitmarsh, R. B., G. Manatschal, and T. A. Minshull (2001), Evolution of magma-poor continental margins from rifting to seafloor spreading, *Nature*, *413*, 150–154.

Wicks, F. J., and D. S. O'Hanley (1988), Serpentine minerals: Structures and petrology, in *Hydrous Phyllosilicates (Exclusive of Micas)*, *Rev. Mineral.*, vol. 19, edited by S. W. Bailey, pp. 91–167.

Wilcock, W. S. D., and J. R. Delaney (1996), Mid-ocean ridge sulfide deposits: Evidence for heat extraction from magma chambers or cracking fronts?, *Earth Planet. Sci. Lett.*, *145*, 49–64.

Wolfe, C., G. M. Purdy, D. R. Toomey, and S. C. Solomon (1995), Microearthquake characteristics and crustal velocity structure at 29°N of the Mid-Atlantic Ridge: The architecture of a slow-spreading segment, *J. Geophys. Res.*, *100*, 24,449–24,472.

M. Cannat, J. Escartin, and F. Fontaine, Equipe de Géosciences Marines, CNRS-UMR7154, Institut de Physique du Globe, 4 Place Jussieu, F-75252 Paris Cedex 05, France. (cannat@ipgp.jussieu.fr)

Author Query Form

(Queries are to be answered by the Author)

2008GM000760 – AGU Rona

The following queries have arisen during the typesetting of your manuscript. Please answer these queries.

Query Marker	Query	Reply
Q1	Please confirm if "t" used all throughout for "ton" is a metric ton or not.	
Q2	Please provide a maximum of 6 keywords.	
Q3	Please check all mentions of Figure 3 and Figure 3 parts for accuracy.	
Q4	Check Table 2 footnotes for accuracy.	
Q5	A degree symbol was inserted here. Please check if appropriate.	
Q6	Please provide the family names of authors S. M. and R. I.	

Thank you very much.